NASA Contractor Report 3702

Contributions of Divergent and Nondivergent Winds to the Kinetic Energy Balance of a Severe Storm Environment

Peter A. Browning and Henry E. Fuelberg

CONTRACT NAS8-33370
JUNE 1983

25th Anniversary
1958-1983

NASA

NASA Contractor Report 3702

Contributions of Divergent and Nondivergent Winds to the Kinetic Energy Balance of a Severe Storm Environment

Peter A. Browning and Henry E. Fuelberg
Saint Louis University
Saint Louis, Missouri

Prepared for
George C. Marshall Space Flight Center
under Contract NAS8-33370

National Aeronautics
and Space Administration

**Scientific and Technical
Information Branch**

1983

ACKNOWLEDGMENTS

The authors thank Dr. Gandikota V. Rao and Dr. Yeong-jer Lin for their suggestions and comments through the course of the investigation. Appreciation is also expressed to the atmospheric energetics research staff, in particular, Dennis Buechler, Mark Fenbers, Paul Meyer, Matt Printy and Mark Ruminski for their technical support and drafting of the figures. The manuscript was expertly typed by Reeder Waters Wade.

This research was supported by the National Aeronautics and Space Administration under contract number NAS8-33370, under the auspices of the Atmospheric Sciences Division, Space Sciences Laboratory, Marshall Space Flight Center, Alabama.

TABLE OF CONTENTS

TABLE OF CONTENTS (Continued)

LIST OF TABLES

LIST OF TABLES (Continued)

LIST OF FIGURES

LIST OF FIGURES (Continued)

1. STATEMENT OF THE PROBLEM

a. Introduction

The development of severe storms is influenced by interactions between scales of motion that range from planetary systems down to the microscale. Recent studies have focused on mechanisms that produce areas of intense convection, characteristics of the severe storm environment, and possible "feedback" mechanisms from the convection to the larger-scale surroundings. Although feedback mechanisms are thought to modify synoptic-scale storm environments, they are not yet fully understood. Diagnostic studies of environmental kinematic parameters and the environmental kinetic energy balance are ways of examining scale interactions and feedback mechanisms in the severe storm environment. This report presents results from such a study.

b. Previous studies

1) Storm-environment interactions

Interactions between convection and the surrounding larger-scale environment have been investigated for many years; however, most advances have been made only recently. Aubert (1957) used numerical models to show that latent heat release

associated with thunderstorms produced increased large-scale, low-level convergence and enhanced upper-level divergence. The synoptic-scale storm environment experienced low-level height falls and upper-level height rises. The effects of latent heat release on changes in pressure patterns have been described by Manabe (1956). Latent heat release was found to enhance the production of kinetic energy (Danard, 1964, 1966) because induced ageostrophic flow was directed toward decreasing pressure in both upper and lower levels. Ninomiya (1971a and b) used conventional rawinsonde data and satellite imagery to detect a mid-tropospheric warm core, strong low-level convergence, and strong upper-level divergence near tornado producing thunderstorms. The formation of a mid-tropospheric jet stream near the storm area was attributed to the increased horizontal temperature gradient caused by the warm core.

A recent surge of interest has developed concerning possible feedback mechanisms from areas of large, and relatively long-lasting, intense storms. Based on enhanced infrared satellite imagery, Maddox (1980a and b) defined the Mesoscale Convective Complex (MCC) to be a nearly circular cloud shield encompassing intense convection lasting at least 6 h. The area of the shield exceeds that of typical individual thunderstorms by two orders of magnitude. Convectively driven, mesoscale circulations were hypothesized to be dominant within the MCC in contrast to larger scale features which control prefrontal squall lines. Environmental conditions associated with the

storm complexes have been described by Maddox (1979), Fritsch and Maddox (1980), Maddox et al. (1981), and Fritsch and Maddox (1981a). The most significant feature of the MCC was an area of mid-tropospheric warming and mean mesoscale ascent. In addition, meso α-scale regions of high pressure and associated anticyclonic flow were observed in the upper troposphere. Jet maxima, whose winds often were 20 m s^{-1} greater than those predicted by the National Weather Service's Limited Fine Mesh Model (LFM), formed on the poleward side of the complexes. Synoptic-scale divergence over the storm area was typically 15 x 10^{-5} s^{-1}. These environmental changes were attributed to the storms; however, the exact physical mechanisms involved require further study. A significant point of the investigations was that current numerical forecasting models do not effectively simulate the major large-scale modifications associated with MCC's because of our incomplete understanding of their complex nature. Other recent diagnostic studies that have described mean, mesoscale ascent in response to convective storms include those by Fankhauser (1969, 1974), Sanders and Paine (1975), Sanders and Emanuel (1977), and Ogura and Chen (1977). It is noteworthy that numerical simulations have duplicated some of the modifications attributed to severe storms (e.g., Rao and Hassebrock, 1972; Kreitzberg and Perkey, 1977; Fritsch and Chapell, 1980a and b; Fritsch and Maddox, 1981b); however, a great deal more remains to be learned before the effects of large, intense areas of convection can be included in the prediction models.

2) Kinetic energy analyses of the total flow

Energy levels of the general circulation, together with the various sources, sinks, and transformations of energy, have been studied extensively (e.g., Dutton and Johnson, 1967; Newell et al., 1970; Saltzman, 1970; Peixóto and Oort, 1974; Oort and Peixóto, 1974). Other investigations have examined the energetics of more limited regions, especially extratropical cyclones. Smith (1980) presents an excellent review of cyclone energetics in which he notes that such systems are energetically active components of the general circulation. Individual cyclones often were found to exhibit major departures from the average.

Large areas of intense convection can be associated with cyclone activity or, in the case of MCC's, can occur without major large-scale forcing mechanisms. In either case, the larger-scale energetics of the convective environment have received relatively little attention. Fuelberg and Scoggins (1978) described the synoptic-scale kinetic energy balance of two large storm areas occurring during NASA's fourth Atmospheric Variability Experiment (AVE 4, 24-25 April 1975). Although no major cyclone activity was present, the various kinetic energy transformations and transports were quite intense. In fact, the storm areas appeared to influence the general circulation as much or more per unit area than intense cyclones. With the aid of the special 3 h rawinsonde data, they observed major fluctua-

tions in energy balance that seemed related to the life cycles of the intense convection within the region. Similarly, Robertson and Smith (1980) found major kinetic energy activity in the extratropical cyclones that produced the Jumbo (3-4 April 1974) and Palm Sunday (10-11 April 1965) tornado outbreaks. Companion studies determined that latent heat release associated with intense convection provided the greatest source of available potential energy to the areas (Lin and Smith, 1979; Smith and Lin, 1980). An intriguing new hypothesis is that widespread convection can act as a source of synoptic-scale kinetic energy. Studies by Kornegay and Vincent (1976), Sheu and Smith (1977), and Vincent and Schlatter (1979) suggest that convection plays a role in the transfer of kinetic energy from unresolvable (subgrid) to resolvable (grid) scales of motion which appears in the "dissipation" term of the kinetic energy balance equation.

Very few kinetic energy studies have been conducted on the subsynoptic scale, mainly due to the lack of appropriate data. McInnis and Kung (1972), Kung and Tsui (1975), and Tsui and Kung (1977) used meso β-scale rawinsonde data (station spacing of 80 km) from the National Severe Storms Laboratory (NSSL) in their investigations. Some energy transformations on this scale were greater than those observed in major synoptic-scale cyclones. The magnitudes of mesoscale energy processes were found to vary greatly, depending on the strength of the convective systems in the area. Time variations in the energy budget terms seemed related to the growth and decay of the nearby storms.

Data from the recent SESAME periods will allow descriptions of mesoscale atmospheric phenomena since the average spacing of the rawinsonde network was either 250 km (regional scale) or 100 km (storm scale). Carlson et al. (1980) and Moore and Fuelberg (1981) have described the rapid changes in horizontal wind, divergence, vertical motion, and stability that occurred in conjunction with the deadly Red River Valley tornado outbreak of 10-11 April 1979. Fuelberg et al. (1980) described the kinetic energy balance of the synoptic-scale storm environment based on National Weather Service (NWS) sonde data alone, while Jedlovec and Fuelberg (1981) performed a similar analysis using both NWS and special site data such that meso α-scale resolution was obtained. Area averaged energetics at individual observation times showed that the energy balance during periods of maximum convective activity differed considerably from that of the remaining periods. The local kinetic energy balance over Oklahoma during the formation of a limited upper-level wind maximum received special attention. Cross-contour production of kinetic energy was found to be the dominant local source for its development. This raised the possibility that the intense convection associated with the Red River Valley Outbreak may have contributed to the formation of the wind maximum.

3) Kinetic energy analyses of divergent and rotational components

A different approach to studying storm-environment interactions is to evaluate the energetics of the divergent and rotational wind components, $\vec{V}_D$ and $\vec{V}_R$, respectively. Such an approach may further explain the mechanisms by which intense thunderstorms modify their larger-scale environments and how such alterations might be included in the numerical forecast models. Diagnostic studies of this type are quite rare, however.

Chen and Wiin-Nielson (1976) have shown that available potential energy is converted into kinetic energy of the divergent wind (K_D) and then into kinetic energy of the rotational component (K_R). Quantity K_D was found to be very important because all of the converted available potential energy goes through K_D which remains small and thereby plays a catalytic role in the conversion process. Northern Hemispheric summertime data showed that K_D/K_T = 10% (K_T is the total kinetic energy) with a maximum near the level of the jet stream in middle latitudes. Krishnamurti (1971) and Chen (1980) showed that $\vec{V}_R$ is the dominant part of the flow at 200 mb in the tropics. Chen et al. (1978), who studied a major mid-latitude cyclone, found that although K_D/K_T = 2.5%, $\vec{V}_D$ assumed crucial importance in the generation and horizontal transport of kinetic energy. Similarly, Smith (1974) noted that alterations to the divergent wind

produced significant changes in station values of total kinetic energy generation and horizontal flux divergence. On the other hand, Krishnamurti (1968) determined that much of the cross-contour flow near a developing wave cyclone could be explained by $\vec{V}_R$ and was attributable to differential vorticity advection and the Laplacian of thermal advection.

c. Objectives

The overall goal of this research is to investigate the roles of the divergent and rotational wind components in the kinetic energy budget of a severe storm environment. A diagnostic study is performed to obtain the synoptic-scale kinetic energy balance of two large storm areas that occurred during NASA's AVE 4 period (24-25 April 1975). Synoptic conditions during AVE 4 and the energetics of the total flow have been studied previously (e.g., Fuelberg and Scoggins, 1978; Maddox, 1980 a and b; Maddox et al., 1981). Apparently, however, relative contributions of the divergent and rotational wind components to total kinetic energy have not been evaluated during any period of intense convection. The following points will be investigated:

1) Space variabilities of $\vec{V}_R$, $\vec{V}_D$, K_R and K_D,

2) Time variabilities of these quantities,

3) Contributions of $\vec{V}_R$ and $\vec{V}_D$ to the kinetic energy balance, and

4) Error bounds for all derived results.

2. THEORETICAL CONSIDERATIONS

The kinetic energy equation for a fixed, limited volume in isobaric coordinates is given by Smith (1969) as:

$$\partial K_T/\partial t = \int\int -\vec{V}\cdot\vec{\nabla}\phi - \int\int \vec{\nabla}\cdot k\vec{V} - \int\int \partial\omega k/\partial p + D + \int k_o \, \partial p_o/\partial t \quad , \quad (1)$$

(A) (B) (C) (D) (E)

where

$\int\int = 1/g \int\int\int dx\, dy\, dp$,

$\vec{V}$ is the horizontal wind vector,

ω is the vertical motion in isobaric coordinates,

$k = (u^2 + v^2)/2$ is the horizontal kinetic energy per unit mass,

$K_T = \int\int k$,

$\phi = gz$ is the geopotential height,

A is the computational area, and

subscript o denotes surface values.

On the right hand side of (1), term A represents generation of kinetic energy due to cross-contour flow while terms B and C represent horizontal and vertical flux divergence of kinetic energy, respectively. Term D is computed as a residual to (1) and represents both thermodynamic and mechanical frictional processes as well as transfers of energy between resolvable and unresolvable scales of motion. This term also contains possible errors arising from all other terms of the equation and is commonly referred to as the "dissipation" term. Term E repre-

sents variations in kinetic energy due to changes in the mass of the volume under consideration. Since it is several orders of magnitude smaller than the other terms in (1), it will not be considered further. In regions of large pressure change, the term could be significant; however, this is not observed during the AVE 4 period.

To examine contributions of the divergent and rotational wind components to the total kinetic energy balance, these components must be introduced into (1). A summary of the Chen et al. (1978) derivation for that purpose follows.

Helmholtz's theorem states that the horizontal velocity ($\vec{V}$) can be expressed as the sum of the divergent wind ($\vec{V}_D$) and the nondivergent or rotational wind ($\vec{V}_R$), i.e.,

$$\vec{V} = \vec{V}_R + \vec{V}_D. \tag{2}$$

Kinetic energy per unit mass is given by

$$k = \tfrac{1}{2}\,\vec{V}\cdot\vec{V} = k_R + k_D + \vec{V}_R\cdot\vec{V}_D, \tag{3}$$

where

$$k_R = \tfrac{1}{2}\,\vec{V}_R\cdot\vec{V}_R \text{ and } k_D = \tfrac{1}{2}\,\vec{V}_D\cdot\vec{V}_D. \tag{4}$$

Using (2), the integrands of terms A and B in (1) can be written as

$$-\vec{V}\cdot\vec{\nabla}\phi = -\vec{V}_R\cdot\vec{\nabla}\phi - \vec{V}_D\cdot\vec{\nabla}\phi \quad , \tag{5}$$

$$-\vec{\nabla}\cdot k\vec{V} = -\vec{\nabla}\cdot k\vec{V}_R - \vec{\nabla}\cdot k\vec{V}_D \quad , \tag{6}$$

Equations (5) and (6) show that horizontal flux divergence and generation of kinetic energy, respectively, are due to both the

divergent and nondivergent wind components. Terms $-\vec{V}_R \cdot \vec{\nabla}\phi$ and $-\vec{V}_D \cdot \vec{\nabla}\phi$ often are denoted as the generation of kinetic energy due to barotropic and baroclinic processes, respectively (Chen and Wiin-Nielson, 1976). Using (5) and (6), (1) can be rewritten as

$$\partial K_T/\partial t = \int\int -\vec{V}_R \cdot \vec{\nabla}\phi + \int\int -\vec{V}_D \cdot \vec{\nabla}\phi - \int\int \vec{\nabla} \cdot k\vec{V}_R$$

$$- \int\int \vec{\nabla} \cdot k\vec{V}_D - \int\int \partial\omega k/\partial p + D \ . \qquad (7)$$

The emphasis of this research is to describe the relative contributions of $\vec{V}_R$ and $\vec{V}_D$ to kinetic energy content in (3), horizontal flux divergence in (5), and generation of kinetic energy in (6).

3. DATA AND COMPUTATIONS

a. Data

The case being investigated is the National Aeronautics and Space Administration's (NASA) fourth Atmospheric Variability Experiment (AVE 4), conducted on 24-25 April 1975. The AVE 4 period has been widely studied because it contains two severe storm outbreaks (e.g., Wilson, 1976; Fuelberg and Scoggins, 1978; Maddox, 1980a and b; Maddox et al., 1981). Rawinsonde data from 42 National Weather Service (NWS) stations were taken at nine times - 24 April at 0000 GMT, 0600 GMT, 1200 GMT, 1500 GMT, 1800 GMT, and 2100 GMT, and on 25 April at 0000 GMT, 0600 GMT, and 1200 GMT. Locations of these stations are shown in Fig. 1. The rawinsonde data were given at 25 mb intervals by Fucik and Turner (1975) while the data reduction procedures used on this set have been described by Fuelberg (1974).

All rawinsonde soundings were checked carefully to determine if sondes had entered violent thunderstorm updrafts or downdrafts. Nonhydrostatic accelerations such as thunderstorm updrafts are a potential source of error since hydrostatic equilibrium is assumed. Data for four soundings (HTS - 1800 GMT; TOP - 0600 GMT; UMN - 1200 GMT; and DAY - 0600 GMT, 24 April) that experienced severe drafts were removed from the data set.

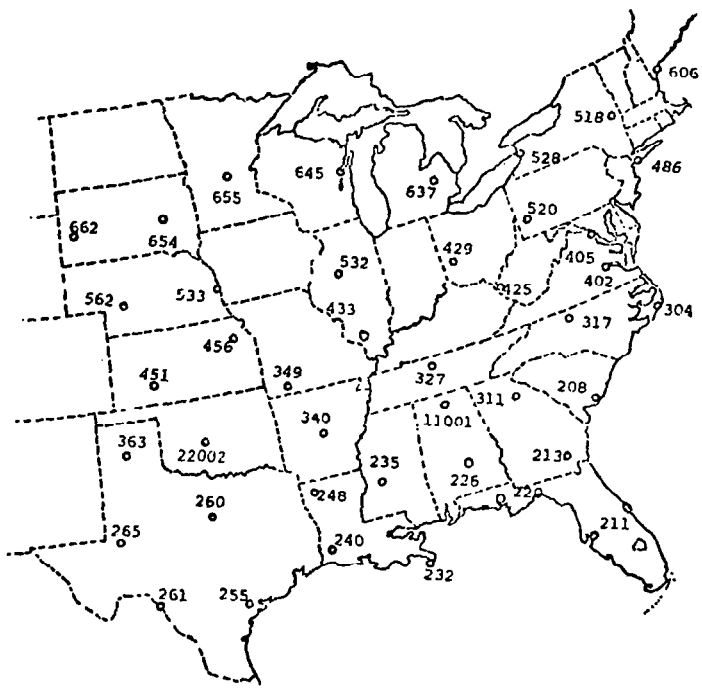

Fig. 1. Rawinsonde stations participating in the AVE 4 experiment.

Surface data from 310 stations were obtained from the National Climatic Center and used in the investigation.

Manually Digitized Radar (MDR) data were obtained from the National Oceanic and Atmospheric Administration's (NOAA) Techniques Development Laboratory to determine objectively the intensity and location of the radar-observed convection. During 1975 MDR data were coded with a single digit from 0 to 9 to indicate areal coverage and echo intensity within blocks that were approximately 83 km on a side. Table 1 defines the MDR code. Plots of MDR values were made each hour for 3 h periods centered on each of the nine rawinsonde observation times. The three hourly plots then were combined into a single chart for each of the nine times by using the highest coded value reported for individual MDR blocks.

b. Analytical procedures

1) Objective analysis

An objective analysis scheme by Barnes (1964) was used to interpolate data from the randomly spaced rawinsonde and surface stations to equally spaced grid points. The grid network, centered over the AVE 4 area, had a spacing of 158 km. Data from each rawinsonde site influenced grid points within a scan radius of three grid distances while four iterations were allowed. The surface data were analyzed using a scan radius of two grid

Table 1. Manually digitized radar (MDR) data code (Foster and Reap, 1973).

Code No.	Maximum Observed VIP Values	Coverage In Box	Maximum Rainfall Rate (in h^{-1})	Intensity Category
0	No Echoes			
1	1	Any VIP1	< 0.1	Weak
2	2	$\leq$ 50% of VIP2	0.1-0.5	Moderate
3	2	> 50% of VIP2	0.5-1.0	Moderate
4	3	$\leq$ 50% of VIP3	1.0-2.0	Strong
5	3	> 50% of VIP3	1.0-2.0	Strong
6	4	$\leq$ 50% of VIP3 and 4	1.0-2.0	Very Strong
7	4	> 50% of VIP3 and 4	1.0-2.0	Very Strong
8	5 or 6	$\leq$ 50% of VIP3, 4, 5, and 6	> 2.0	Intense or Extreme
9	5 or 6	> 50% of VIP3, 4, 5, and 6	> 2.0	Intense or Extreme

distances with four iterations. Even though the resulting objectively analyzed fields agreed well with subjectively (hand-analyzed) data fields, a mild filter by Shuman (1957) was applied to the grids to further suppress features below the minimum data resolution (twice the station separation). The smoothing element index used in this procedure was 0.2.

Gridded analyses of height, temperature, wind components, and moisture content were produced at 18 levels, i.e., the surface and at 50 mb intervals from 900 mb to 100 mb for each of the nine times. Winds at the 18 levels were arithmetic averages over 50 mb layers to reduce the effects of random errors that are inherent in the data. The grids resulting from the above procedures are identical to those employed by Wilson (1976) and Fuelberg and Scoggins (1978).

2) Computation of divergent and nondivergent winds

An iterative scheme developed by Endlich (1967) and used by Chen et al. (1978) was employed to separate the horizontal wind into its divergent and rotational components. This scheme allows the divergence to be virtually eliminated while conserving the original vorticity. A brief description of this method follows.

First, vorticity is calculated using centered finite differences on the original analyzed wind components. To reduce the divergence at a given grid point to zero, adjustments of

equal magnitude, but opposite sign, are made to the u and v wind components at the neighboring grid points. While reducing the divergence, the procedure modifies the vorticity of the resulting wind. Therefore, to retain the original vorticity, u and v in the vicinity of the grid point in question are modified appropriately. Then at the next grid point, the most recent winds are used. The procedure continues until all grid points are handled; then the second iteration begins. With repeated application of this procedure, the divergence of the adjusted wind approaches zero while its vorticity remains that of the original wind. For our purposes, the divergence of the adjusted wind field was everywhere reduced to at least 1×10^{-7} s^{-1}, which is less than 0.1% of the largest magnitudes in the original winds (1.4×10^{-4} s^{-1}). Thus, the final field can be considered to be nondivergent in character. A constant correction was added to the u and v components of the nondivergent winds so that average values agreed with those of the original components. Similar corrections were made by Endlich (1967) and Chen et al. (1978). Finally, the divergent wind was obtained as the difference between components of the nondivergent and the original winds.

An alternative technique for computing rotational and divergent winds is the solution of Poisson equations for stream function and velocity potential (Charney, 1962). This procedure was investigated for use here. The need for specifying meteorologically satisfactory boundary conditions in solving the Poisson equations meant a considerable loss of area on the periphery of

the AVE 4 region. Also, computational limitations initially resulted in a 30% loss of divergence when compared with values obtained from the original winds. Although later use of a staggered grid network was successful in retaining original divergence, it required that the divergent and nondivergent winds be interpolated back onto the original grid before solution of the kinetic energy budget equation. Because of its simplicity and accurate results, the Endlich procedure was utilized in this study.

3) Computation of vertical motion

The kinematic method was used for computing vertical motion. As the lower boundary condition, a value of zero was assumed at the surface. A limitation of the kinematic method is that errors in the computation of divergence accumulate by the end of the integration process, causing unrealistic values of vertical motion near 100 mb. To reduce this problem, the scheme suggested by O'Brien (1970) was used to adjust the profile of ω to zero at 100 mb. Adjusted values of divergence were not used in the calculation of $\vec{V}_D$.

4) Finite differencing and integration

Centered finite differences were used to compute horizontal derivatives, and all vertical derivatives except those at the

surface and at 100 mb where noncentered differences were employed. Time derivatives also were evaluated using centered differences where possible, but uncentered differences at the first and last time were required.

Terms of the kinetic energy budget equation (7), except dissipation, were computed at each grid point for each of the 18 levels and then integrated over 50 mb layers from the surface to 100 mb using the trapezoidal rule. The dissipation term was computed as a residual to balance (7) at each grid point in each 50 mb layer.

c. Error analysis

Rawinsonde data contain errors which influence all subsequent calculations to varying degrees (Kurihara, 1961). To obtain quantitative confidence limits for the kinetic energy budget terms of the present study, separate computations were performed using randomly perturbed data. The procedures utilized in this analysis, as well as detailed results, are presented in the Appendix. Generally, however, errors in rawinsonde data should not seriously affect the interpretations of results that follow. One should exercise some discretion in assigning significance to minor term fluctuations, especially in the upper levels.

4. SYNOPTIC CONDITIONS

Although the AVE 4 period was characterized by weak pressure and frontal activity, two large areas of intense convection occurred. Both of these areas have been classified as Mesoscale Convective Complexes (MCC's) (Maddox, 1979). By the end of the 36 h period, eight people had died and at least fifty injured as a result of a dozen tornadoes, wind damage, and flash flooding.

Since detailed descriptions of weather conditions during AVE 4 have been given by Fuelberg and Scoggins (1978), Maddox (1979), and Maddox et al. (1981), only a brief discussion of the major synoptic-scale features will be presented here. At 0000 GMT 24 April (Fig. 2), the upper troposphere was characterized by a poorly defined polar jet stream over the northern United States and a subtropical jet along the Gulf Coast States. Intense thunderstorms (Fig. 3) were occurring over Kansas, Missouri, and Illinois in response to a weak short-wave trough in the middle troposphere (Fig. 2). Strongest thunderstorms were located at the nose of a weak speed maximum in the polar jet stream. No pronounced diffluence was evident over the AVE 4 area at this time.

By 0600 GMT (not shown), definite changes had occurred on the synoptic scale. The thunderstorms had organized into the first MCC of the period (Fig. 3). Rapid storm development had occurred eastward of the inital locations as the short-wave trough at 500 mb advanced. Additional formation occurred over

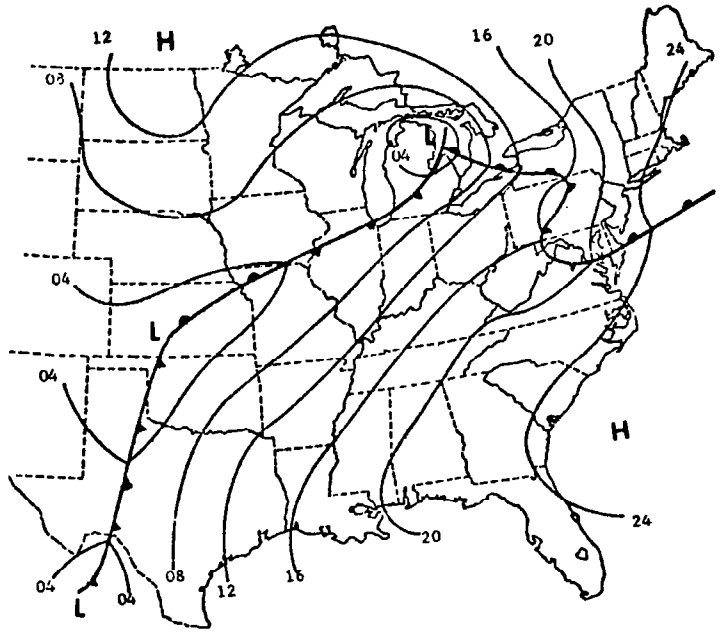

(a) Surface.

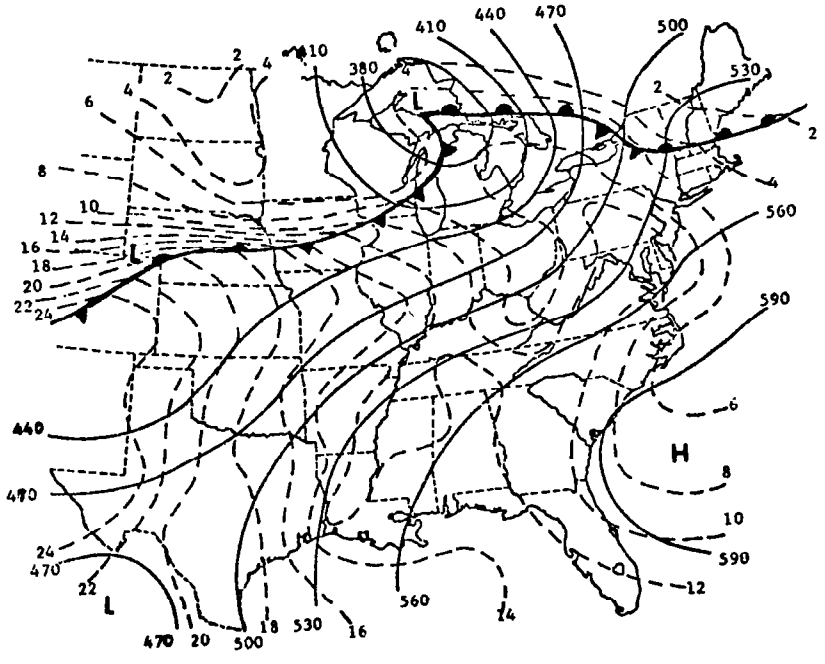

(b) 850 mb.

Fig. 2. Synoptic conditions at 0000 GMT 24 April 1975 (Fucik and Turner, 1975).

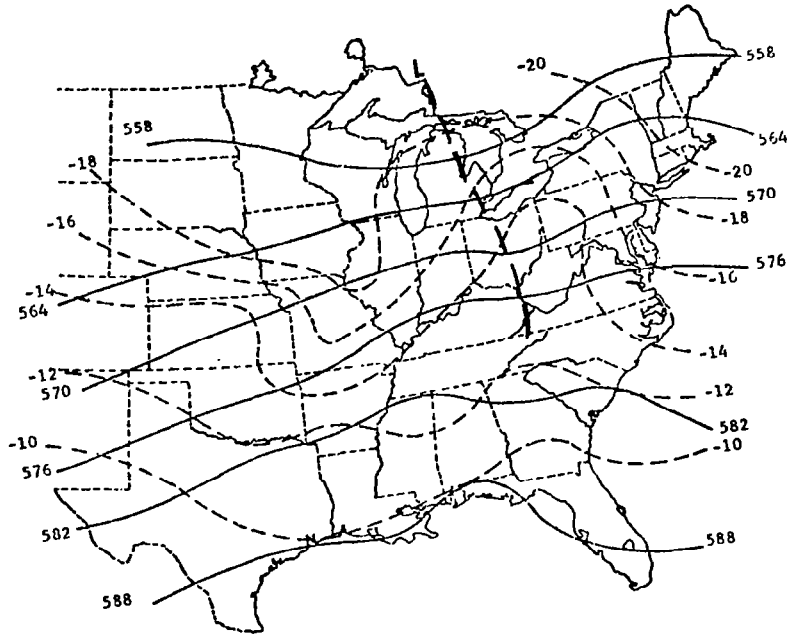

(c) 500 mb.

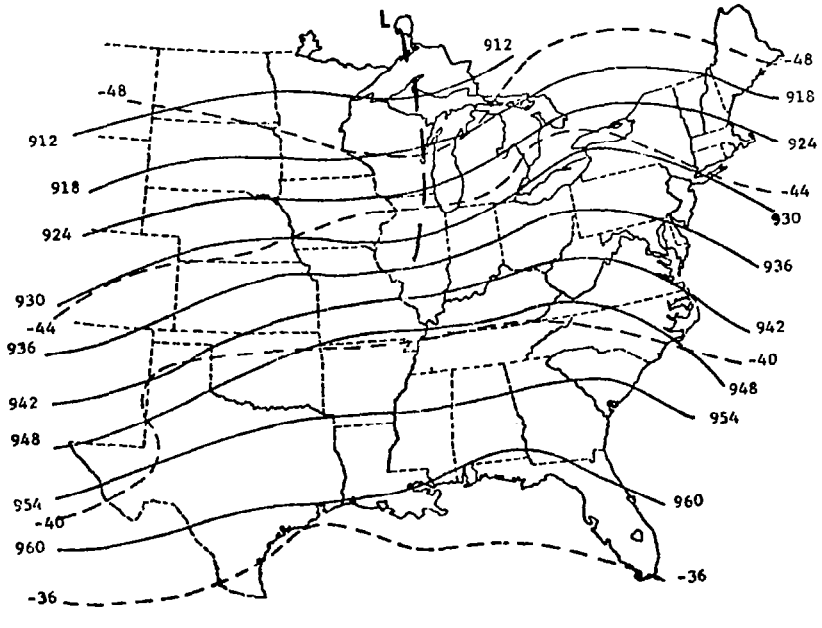

(d) 300 mb.

Fig. 2. (Continued).

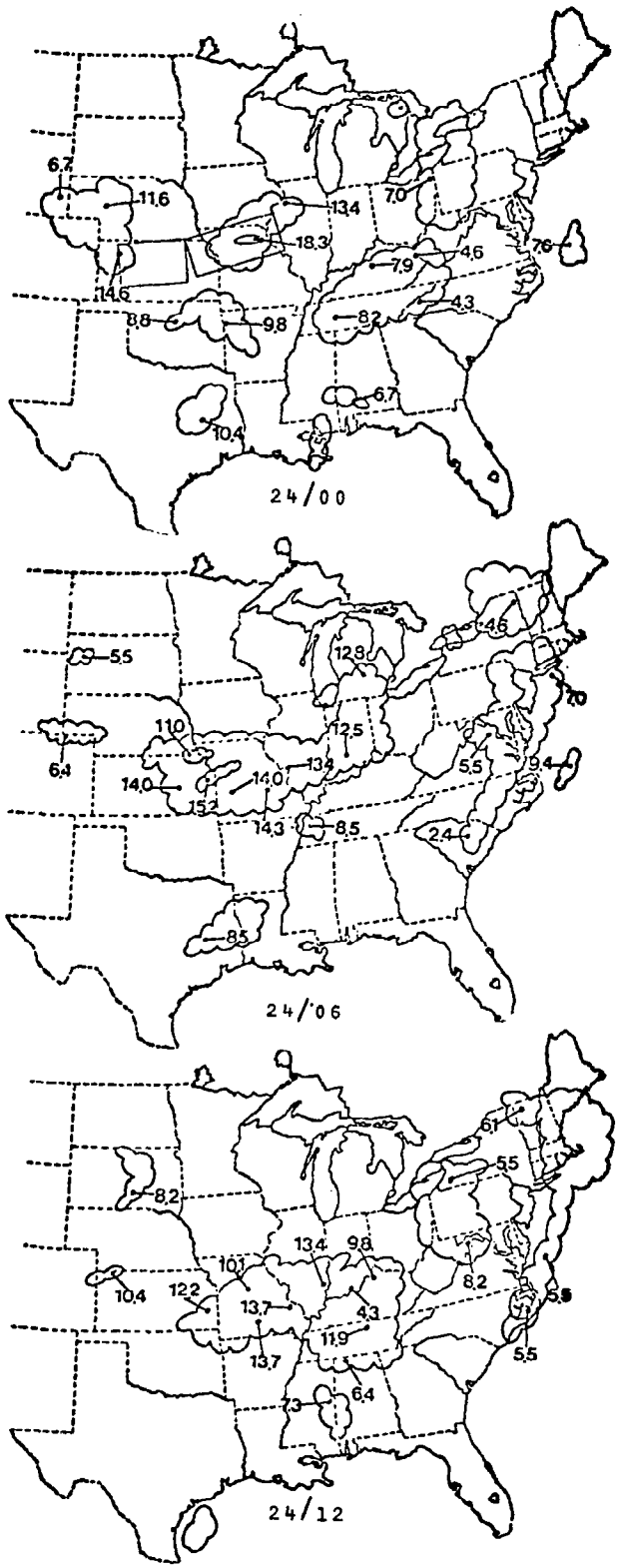

Fig. 3. National Meteorological Center radar summaries for the first storm outbreak. Echo tops are in kilometers.

Kansas. At jet stream level, the polar jet became much stronger along the northern edge of the convection. Speeds had increased as much as 15 m s^{-1} during the previous 6 h period over Illinois and Indiana, and now were as great as 65 m s^{-1}. Speeds had decreased south of the MCC. Pronounced diffluence in the polar jet now was evident over northern Missouri, Indiana, and Ohio. These significant changes in synoptic-scale flow patterns are hypothesized to be due to feedback processes from the MCC's to the synoptic scale (Maddox, 1979). Thunderstorm activity remained intense at 1200 GMT (Fig. 3), but the storms weakened to showers by 1500 GMT (not shown) as they moved to the east.

The second MCC initially developed near 2100 GMT. The outbreak began in eastern Kansas along a cold front extending from a low in Kansas, southwestward into Oklahoma (Fig. 4). At 500 mb, a second short-wave trough over the Dakotas caused the surface cyclone in central Kansas to intensify. In the upper troposphere, the subtropical jet was located over Texas and Louisiana with a strong speed maximum over Texas. The polar jet curved from the Texas Panhandle into the northeastern United States. Strongest winds were over Nebraska, with secondary maxima over Illinois and southwest Missouri. A broad band of weakly defined diffluence covered the southeast half of the AVE 4 area. By 0000 GMT 25 April (Fig. 5), a storm complex stretched from Missouri into Oklahoma with maximum radar tops reaching 55,000 ft (16.8 km).

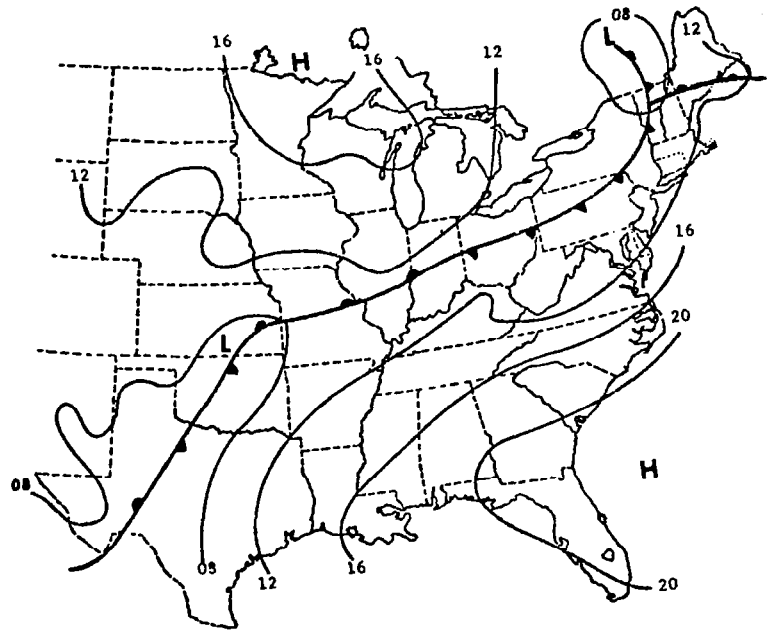

(a) Surface.

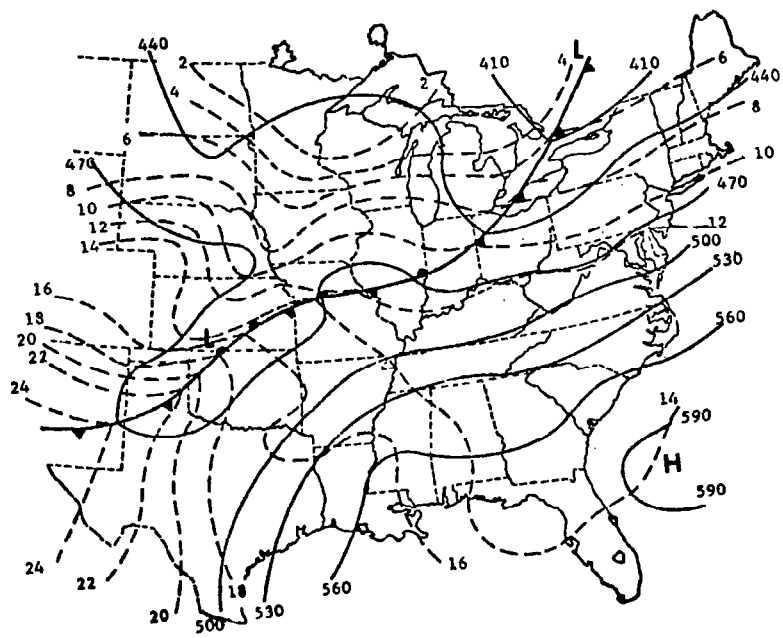

(b) 850 mb.

Fig. 4. Synoptic conditions at 2100 GMT 24 April 1975 (Fucik and Turner, 1975).

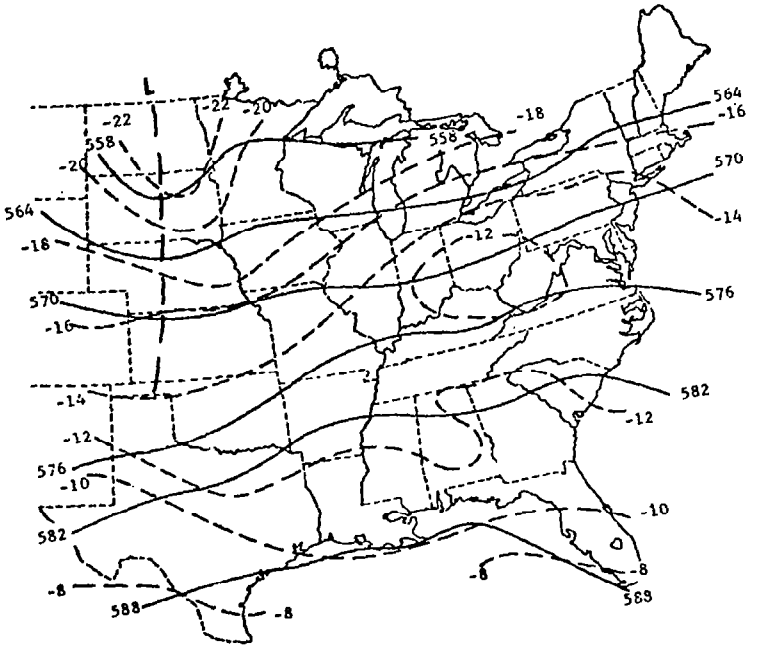

(c) 500 mb.

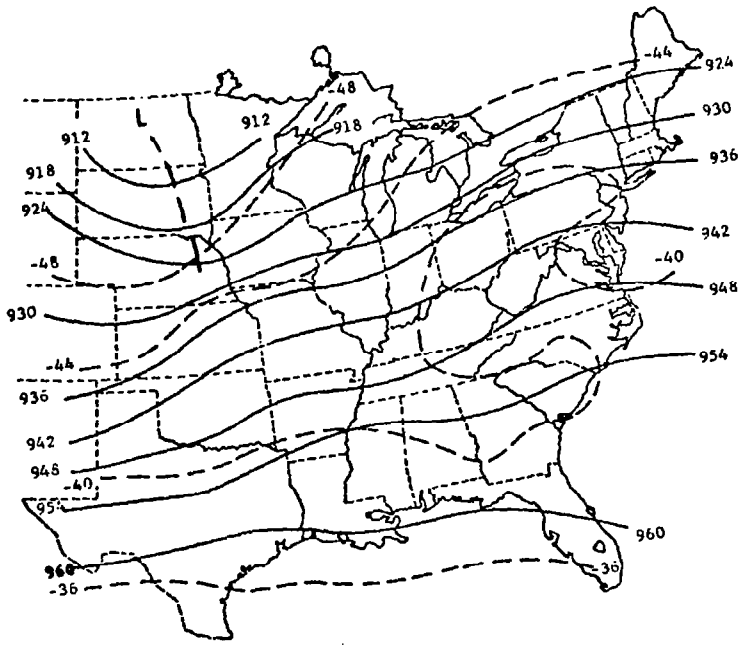

(d) 300 mb.

Fig. 4. (Continued).

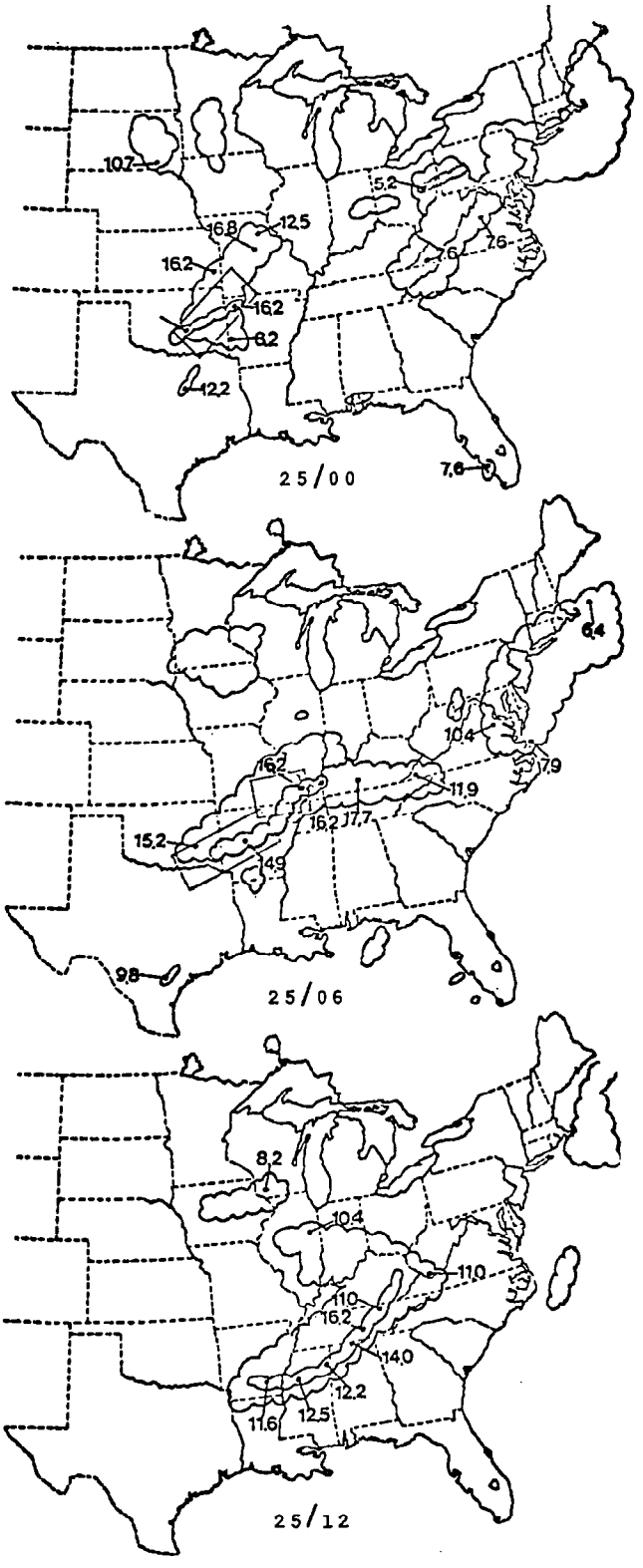

Fig. 5. National Meteorological Center radar summaries for the second storm outbreak. Echo tops are in kilometers.

By 0600 GMT (Fig. 5) the newly formed MCC was located over the Mid-Mississippi Valley. Strongest thunderstorms stretched from eastern Kentucky into eastern Oklahoma, ahead of the short-wave trough at 500 mb. In the upper troposphere (not shown), remarkable changes again had occurred in the flow patterns. Although peak speeds along the subtropical jet had decreased 10 to 20 m s^{-1}, a wind maximum again had developed on the polar jet just north of the strongest radar echoes. Greatest speeds within this area exceeded 65 m s^{-1}, an increase of over 15 m s^{-1} from 6 h earlier. The upper-tropospheric flow now was extremely diffluent over the region of strong thunderstorm activity; peak values of divergence at 200 mb reached 14×10^{-5} s^{-1}.

The MCC had moved southeastward by 1200 GMT (Fig. 5). Radar echoes extended along an arc from eastern Kentucky, into northern Alabama and Arkansas. The polar jet stream remained intense and continued to exhibit strongly diffluent flow over the active storm area (Fig. 6). Its location continued to be along the northern edge of the cirrus shield associated with the thunderstorm complex.

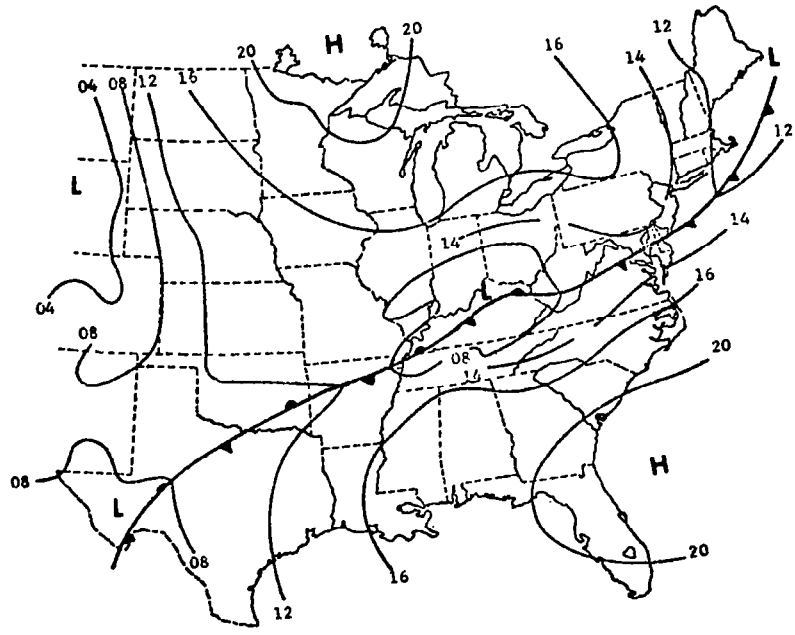

(a) Surface.

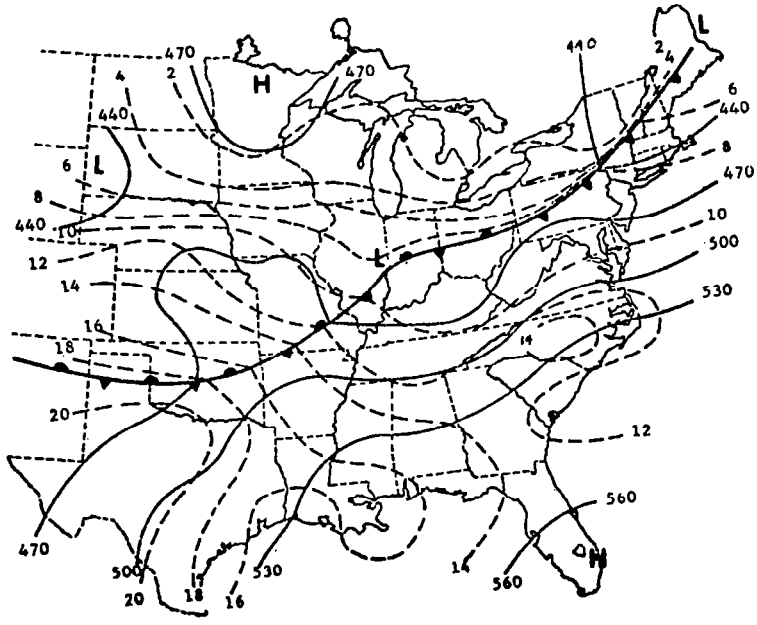

(b) 850 mb.

Fig. 6. Synoptic conditions at 1200 GMT 25 April 1975 (Fucik and Turner, 1975).

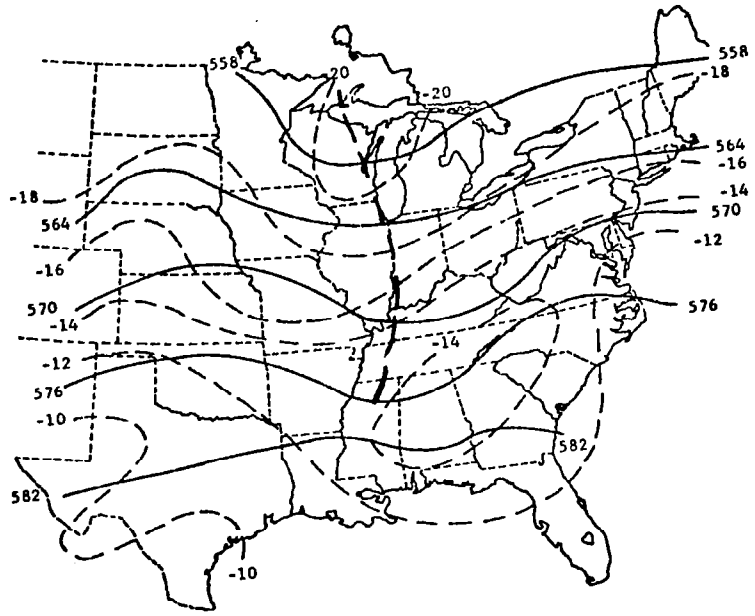

(c) 500 mb.

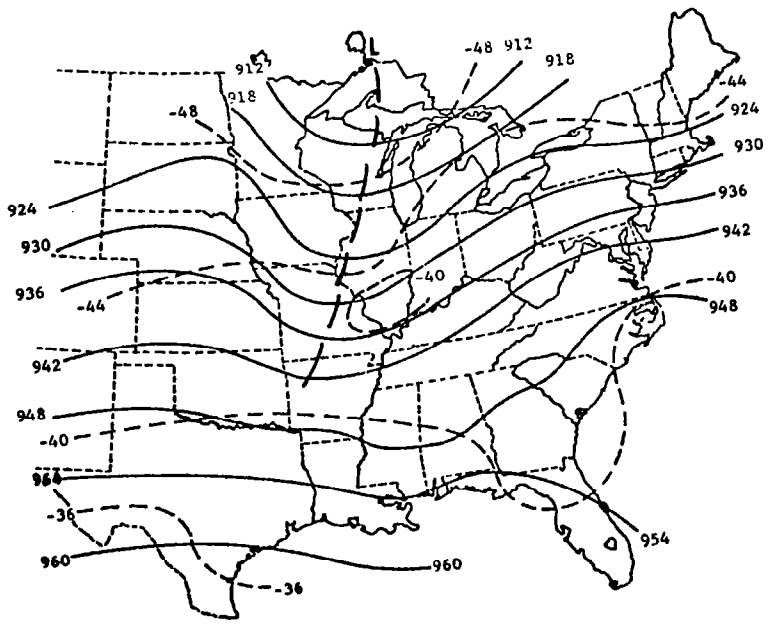

(d) 300 mb.

Fig. 6. (Continued).

5. RESULTS

The energy balance was computed for each observation time over the entire AVE 4 region (Fig. 1). Results for the single times then were averaged over the entire 36 h period. Energy budgets also were compiled for smaller, more limited volumes that moved with the convection. This section begins by giving an overview of the energetics for the entire region. Later sections focus on the energy balances of the smaller subregions. Since Fuelberg and Scoggins (1978) have already described the kinetic energy balance of the total flow, this discussion emphasizes roles of the divergent and nondivergent wind components.

a. Energetics of the composite AVE 4 period

Average energetics of the large-scale flow in which the storms are imbedded is described by the composite budget for all nine observation times. Table 2 gives values for the total flow. Greatest energy content is found between 300-200 mb in association with jet stream activity, but total kinetic energy decreases with time at all levels during the 36 h period. Dissipation to subgrid-scale motions is a major factor producing this decrease below 800 mb where surface friction dominates. However, destruction of kinetic energy due to supergeostrophic cross-contour flow is the largest energy sink in the upper atmosphere (above 600 mb). Vertical flux divergence is found in

Table 2. Area-time averaged kinetic energy budget. All units are W m^{-2} except for K_T which is 10^5 J m^{-2}.

Pressure Layer (mb)	K_T	$\partial K_T/\partial t$	$-\vec{V}_T \cdot \vec{\nabla}\phi$	$\vec{\nabla} \cdot k\vec{V}_T$	$\partial \omega k/\partial p$	D
200-100	4.40	-1.16	-2.98	0.05	-1.42	0.45
300-200	5.41	-0.52	-2.24	1.80	-1.47	2.05
400-300	3.37	-0.25	-1.47	-0.35	0.27	1.14
500-400	2.16	-0.29	-0.81	-0.28	0.29	0.53
600-500	1.54	-0.37	-0.40	0.09	0.44	0.56
700-600	1.07	-0.37	0.19	0.29	0.63	0.36
800-700	0.79	-0.33	0.13	0.09	0.53	0.16
900-800	0.70	-0.44	1.40	-0.05	0.48	-1.41
SFC-900	0.35	-0.24	2.21	0.01	0.25	-2.19
Vertical Total	19.8	-4.0	-4.0	1.6	0	1.6

the lower layers while flux convergence occurs above, thus indicating an upward transport of energy by rising air associated with widespread convection. Horizontal flux divergence of kinetic energy is small through most of the atmosphere except near 250 mb where it provides an important sink. (Here, the sign convention is that positive values of vertical and horizontal flux indicate an outward transport of energy). Positive dissipation is an important energy source above 800 mb, suggesting transfers from subgrid to grid scales of motion.

Table 3 shows the distribution of kinetic energy between the divergent and rotational wind components (K_D, K_R) and term $\vec{V}_R \cdot \vec{V}_D$. Values of the ratio K_D/K_T also are given. Maximum values of K_T, K_R and K_D occur in the 300-200 mb layer, thereby, coinciding with the jet stream. Values of K_R are only slightly smaller than those of K_T. The ratio K_D/K_T is small above 500 mb with a maximum slightly greater than 2%. Below 500 mb, however, values of K_D/K_T increase toward the surface as magnitudes of K_T and K_R diminish. The error in approximating K_T by K_R is always less than 10% during the composite period. Term $\vec{V}_R \cdot \vec{V}_D$ is smaller in magnitude than K_D at all levels and is negative above 900 mb. Its sign and magnitude are dependent on the orientation of the two wind vectors, e.g., negative values occur when the winds oppose each other. Although the term integrates to zero in a global domain, this does not occur when limited regions such as AVE 4 are considered.

Table 3. Components of area-time averaged kinetic energy content. Units of energy are 10^5 J m^{-2}.

Pressure Layer (mb)	K_T	K_R	K_D	$\vec{V}_R \cdot \vec{V}_D$	K_D/K_T
200-100	4.40	4.36	0.06	-0.02	1.4%
300-200	5.41	5.35	0.12	-0.06	2.2%
400-300	3.37	3.32	0.05	0.00	1.5%
500-400	2.16	2.15	0.03	-0.02	1.6%
600-500	1.54	1.53	0.04	-0.03	2.6%
700-600	1.07	1.05	0.04	-0.02	3.7%
800-700	0.79	0.78	0.04	-0.03	5.0%
900-800	0.70	0.66	0.05	-0.01	7.0%
SFC-900	0.35	0.31	0.03	0.01	8.6%
Vertical Total	19.79	19.51	0.46	-0.18	2.3%

Horizontal transport of kinetic energy into and out of the region is represented by the flux divergence term ($\vec{\nabla}\cdot k\vec{V}$). Table 4 presents a vertical tabulation of the divergent and rotational components comprising the total flux. The divergent wind is a source of flux convergence below 700 mb but contributes to flux divergence above 600 mb. Greatest values of $\vec{\nabla}\cdot k\vec{V}_D$ occur at jet stream level. For the most part, horizontal flux due to the rotational wind opposes the contribution of the divergent wind. Term $\vec{\nabla}\cdot k\vec{V}_R$ is a source of flux convergence above 500 mb and flux divergence nearer the surface. Both components yield flux divergence in the midtroposphere. Although Table 3 revealed that K_D is one to two orders of magnitude smaller than K_R, the divergent wind component is as important as the rotational component in contributing to the total horizontal flux. In fact, the divergent component dominates $\vec{\nabla}\cdot k\vec{V}_T$ above 300 mb. The vertically integrated result (Table 4) is that the divergent component provides a major sink of energy to the region, but 64% of this amount is offset by inflow due to the rotational wind.

Components of the cross-contour generation term are given in Table 4 as a function of pressure. As observed with the flux term, the divergent and rotational components produce differing results above 700 mb. The divergent component crosses the contours toward lower values at most levels, thereby generating kinetic energy. The rotational component produces the opposite result above 700 mb. The combined effect is destruction of

Table 4. Components of area-time averaged generation and horizontal flux divergence of kinetic energy. Units are W m^{-2}.

Pressure Layer (mb)	$-\vec{V}_T \cdot \vec{\nabla}\phi$	$-\vec{V}_R \cdot \vec{\nabla}\phi$	$-\vec{V}_D \cdot \vec{\nabla}\phi$	$\vec{\nabla} \cdot k\vec{V}_T$	$\vec{\nabla} \cdot k\vec{V}_R$	$\vec{\nabla} \cdot k\vec{V}_D$
200-100	-2.98	-3.01	0.03	0.05	-1.45	1.50
300-200	-2.24	-2.93	0.69	1.80	-0.78	2.58
400-300	-1.47	-2.13	0.66	-0.35	-0.87	0.52
500-400	-0.81	-1.11	0.30	-0.28	-0.39	0.11
600-500	-0.40	-0.89	0.49	0.09	0.05	0.04
700-600	0.19	-0.25	0.44	0.29	0.29	0.00
800-700	0.13	0.26	-0.13	0.09	0.20	-0.11
900-800	1.40	1.18	0.22	-0.05	0.11	-0.16
SFC-900	2.21	1.21	1.00	0.01	0.08	-0.07
Vertical Total	-4.0	-7.7	3.7	1.6	-2.8	4.4

kinetic energy above 600 mb; however, in the lower troposphere (below 800 mb), both components produce kinetic energy. The vertical totals indicate that generation by $\vec{V}_D$ offsets by 48% the destruction of kinetic energy by $\vec{V}_R$. It is significant that divergent generation provides the only source of kinetic energy to the AVE 4 region during the composite 36 h period.

b. Time variability for the entire area

The special AVE data set allows energy changes at 3 and 6 h intervals to be monitored during the convectively active period. Time variability of the surface-100 mb total flow energy balance is given in Table 5. Since boundary conditions for vertical velocity are zero at both the surface and 100 mb, vertical flux in the column integrates to zero, and therefore is not included. Total kinetic energy decreases with time except at 1200 GMT and 2100 GMT 24 April when slight increases are noted. The time derivative reflects these variations; however, one should recall that centered time differences were used in the computations. Horizontal flux convergence is an energy source at the start of AVE 4 and from 1200 GMT to 2100 GMT 24 April. Strong flux divergence occurs near peak intensities of both MCC's (0600 GMT 24 April and 0600 GMT 25 April) as well as near the end of the experiment.

Destruction of kinetic energy by cross-contour flow provides a major sink between 0600 GMT and 1500 GMT 24 April which

Table 5. Vertical totals of the area averaged kinetic energy budget for individual observation times. All units are W m^{-2} except K_T which is 10^5 J m^{-2}.

Date/Time	K_T	$\partial K_T/\partial t$	$-\vec{V}_T \cdot \vec{\nabla}\phi$	$\vec{\nabla} \cdot k\vec{V}_T$	D
24/00	23.01	-11.39	0.77	- 6.07	-18.23
24/06	20.55	- 5.40	-10.48	8.68	13.76
24/12	20.70	- 3.82	-24.26	- 1.53	18.91
24/15	19.31	- 6.37	-12.77	- 2.43	3.97
24/18	19.31	1.52	9.87	- 3.35	-11.70
24/21	19.65	- 1.17	5.61	- 2.17	- 8.95
25/00	19.07	- 2.29	- 5.84	1.03	4.58
25/06	18.86	- 2.55	2.72	4.68	- 0.59
25/12	18.00	- 4.39	- 1.50	15.85	12.96
Composite	19.8	- 4.0	4.0	1.6	1.6

includes much of the life cycle of the first MCC. Destruction is due to supergeostrophic flow being directed across the contours toward higher pressure. Although weak generation occurs near peak intensity of the second MCC (0600 GMT 25 April), strongest values are found between 1800 GMT and 2100 GMT. Signs of dissipation and generation are opposite at every observation time. During times of cross-contour destruction, kinetic energy is transferred from subgrid to resolvable scales (positive dissipation) and vice versa. Positive dissipation provides a major source of synoptic-scale energy between 0600 GMT and 1500 GMT 24 April as well as at 1200 GMT 25 April.

It is interesting to note that there is little correlation between the kinetic energy balance of the total flow and the life cycles of the two areas of intense convection, at least when the entire region is considered. When budgets for limited volumes enclosing the two MCC's are described in a later section, a clearer relationship will be apparent.

Time variability of kinetic energy partitioned among the divergent and rotational wind components is given in Table 6 for the surface-100 mb layer. Rotational energy remains slightly smaller than K_T until the last observation time, and temporal variations of K_R closely reflect those of K_T. On the other hand, there are two maxima in the divergent component, and both occur at times of peak convective activity. Values of K_D/K_T reveal that K_D comprises between 1.6% and 2.7% of the total energy during periods of little convection. During times of

Table 6. Vertical totals of the area averaged components of kinetic energy content for individual observation times. Units of energy are 10^5 J m^{-2}.

Date/Time	K_T	K_R	K_D	$\vec{V}_R \cdot \vec{V}_D$	K_D/K_T
24/00	23.01	22.54	0.36	0.11	1.6%
24/06	20.55	19.76	0.70	0.09	3.4%
24/12	20.70	20.08	0.48	0.14	2.3%
24/15	19.31	19.03	0.39	-0.11	2.0%
24/18	19.31	19.21	0.35	-0.25	1.8%
24/21	19.65	19.63	0.37	-0.35	1.9%
25/00	19.07	18.98	0.33	-0.24	1.7%
25/06	18.86	18.30	0.85	-0.29	4.5%
25/12	18.00	18.03	0.48	-0.51	2.7%
Composite	19.8	19.5	0.5	-0.2	2.6%

peak MCC activity, however, values of 3.4% and 4.5% are observed for the first and second outbreaks, respectively. Thus, the enhanced divergence associated with the convective storms is evident even when the entire region is considered. Term $\vec{V}_R \cdot \vec{V}_D$ is positive through 1200 GMT 24 April and then becomes negative for the remainder of the AVE 4 experiment. Its magnitude is consistently smaller than that of K_D, except at the final time.

To further examine variability of the two components, pressure-time cross sections are given in Fig. 7. A close correlation exists between the intense convection and the kinetic energy of the divergent wind component. Maximum values of K_D are found in the upper troposphere at 0600 GMT 25 April when the second MCC is most intense. At that time, the divergent component comprises 5.6% of the total energy in the 300-200 mb layer. An upper-level maximum of K_D also is associated with the first MCC at 0600 GMT 24 April. Large values of K_D are attributable to large horizontal divergence at jet stream level which is hypothesized to be induced by the storm outbreak (Maddox et al., 1981). Weaker, secondary maxima appear in the lower troposphere near the times of peak convection. Time variability of K_R (Fig. 7) appears to be more closely related to the larger-scale circulation than to the storm outbreaks. Maximum values are persistently found at the jet stream level (300-200 mb layer).

Contributions of the two components to total generation are shown in Table 7. The divergent component provides a source of kinetic energy to the region at every time. The maximum value

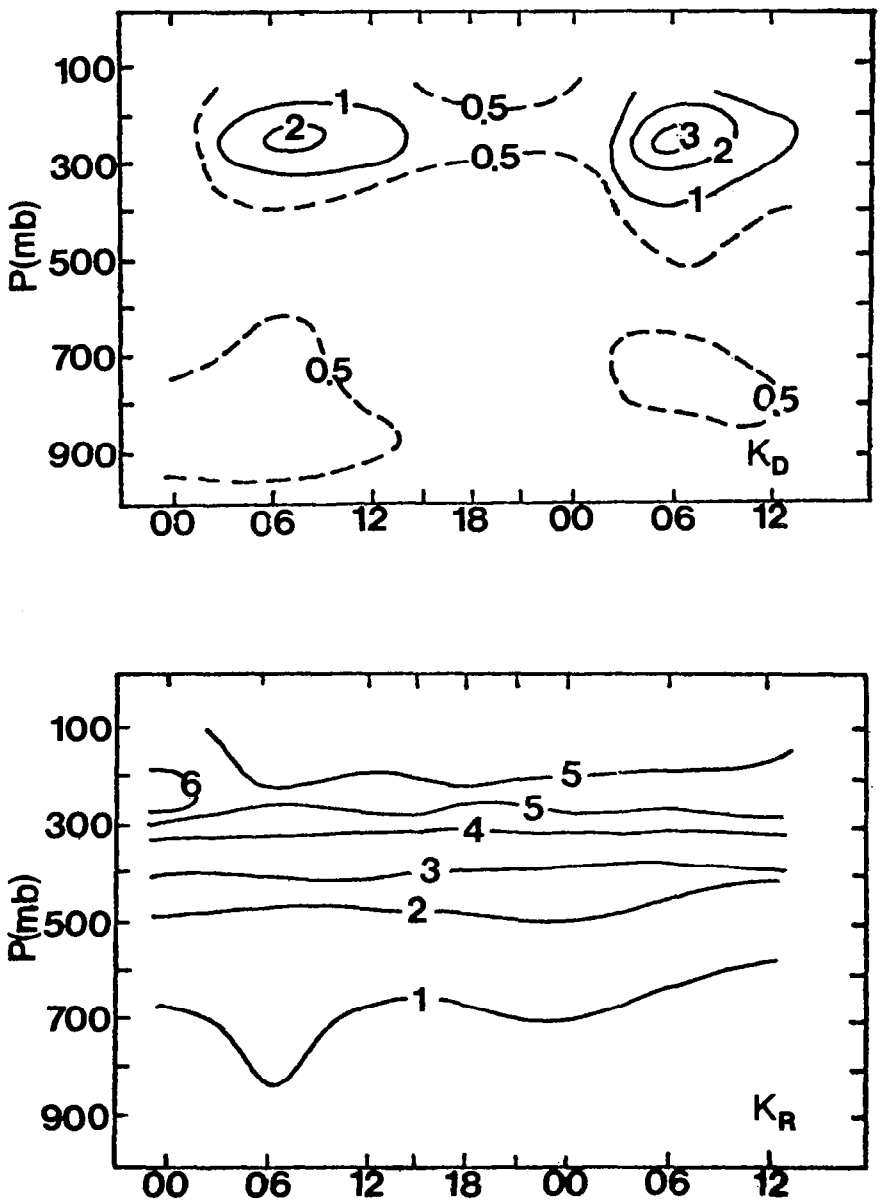

Fig. 7. Pressure-time cross sections of area averaged kinetic energy budget terms. Units of K_D and K_R are 10^4 J m^{-2}/100 mb and 10^5 J m^{-2}/100 mb, respectively; while other units are W m^{-2}/100 mb.

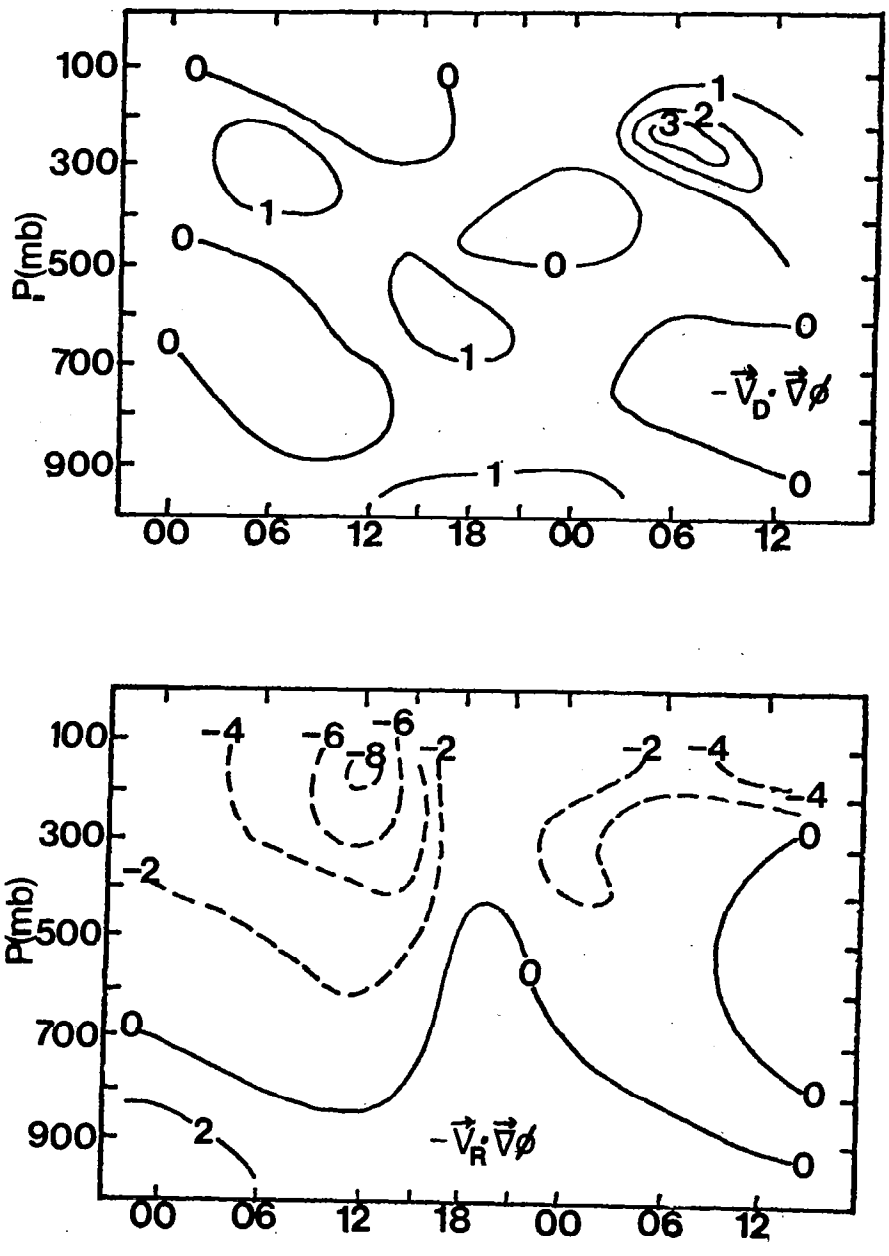

Fig. 7. (Continued).

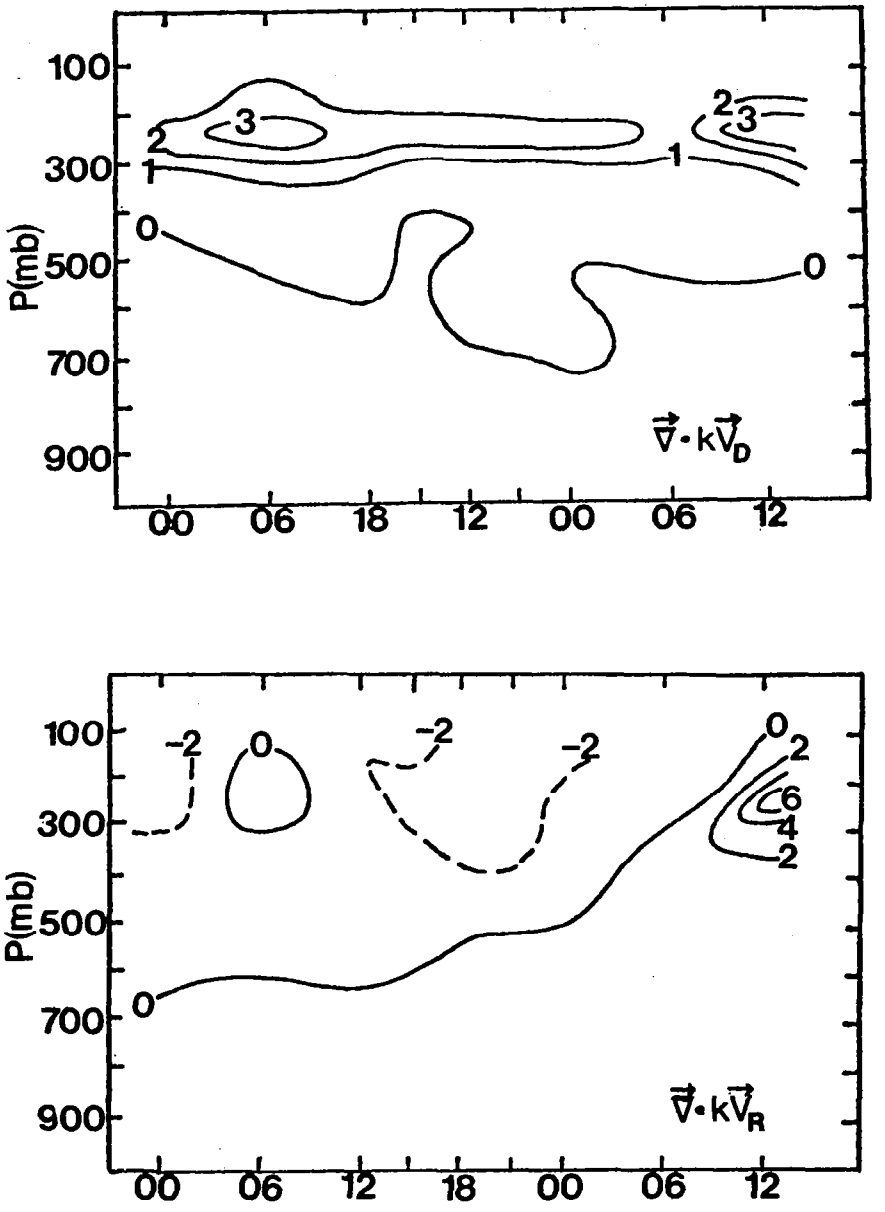

Fig. 7. (Continued).

Table 7. Vertical totals of the area averaged components of generation and horizontal flux divergence for individual observation times. All units are W m^{-2}.

Date/Time	$-\vec{V}_T \cdot \vec{\nabla}\phi$	$-\vec{V}_R \cdot \vec{\nabla}\phi$	$-\vec{V}_D \cdot \vec{\nabla}\phi$	$\vec{\nabla} \cdot k\vec{V}_T$	$\vec{\nabla} \cdot k\vec{V}_R$	$\vec{\nabla} \cdot k\vec{V}_D$
24/00	0.77	- 3.19	3.96	- 6.07	-8.80	2.73
24/06	-10.48	-13.49	3.01	8.68	2.18	6.50
24/12	-24.26	-26.81	2.55	- 1.53	-5.53	4.00
24/15	-12.77	-17.52	4.75	- 2.43	-5.75	3.32
24/18	9.87	4.94	4.93	- 3.35	-7.43	4.08
24/21	5.61	3.01	2.60	- 2.17	-6.33	4.16
25/00	- 5.84	- 7.16	1.32	1.03	-3.44	4.47
25/06	2.72	- 3.99	6.71	4.68	0.46	4.22
25/12	- 1.50	- 4.90	3.40	15.85	9.71	6.14
Composite	- 4.0	- 7.7	3.7	1.6	-2.8	4.4

of 6.71 W m^{-2} occurs near peak intensity of the second outbreak. On the other hand, the rotational wind destroys kinetic energy at most times. The largest negative values occur between 0600 GMT and 1500 GMT 24 April. It is noteworthy that the two components generally are equally important in explaining total generation. This happens in spite of the fact that K_D is much smaller than K_R (Table 6).

The pressure-time cross section for $-\vec{V}_D \cdot \vec{\nabla}\phi$ (Fig. 7) indicates only weak generation and destruction of energy until the second outbreak of convection. At 0600 GMT 25 April, strong generation of kinetic energy occurs within the 300-200 mb layer, and continues through the end of the experiment. Peak values of 3.75 W m^{-2}/100 mb within this layer are similar to those of the total generation (3.53 W m^{-2}/100 mb). Figure 7 also contains the pressure-time cross section of $-\vec{V}_R \cdot \vec{\nabla}\phi$. Strong destruction of kinetic energy is evident above 400 mb throughout the AVE 4 experiment. Maximum destruction occurs in the 100-200 mb layer approximately 6 h after the first MCC reaches peak intensity. As noted in Table 7, total generation is primarily influenced by the rotational wind until the second storm outbreak.

Time variability of total horizontal flux divergence and its two components is given in Table 7. The divergent wind produces a consistent export throughout the period. Maximum values of 6.50 and 6.14 W m^{-2}/100 mb occur at 0600 GMT 24 April and 1200 GMT 25 April, respectively. At peak intensity of the first MCC (0600 GMT 24 April), nearly 75% of the total hori-

zontal flux is due to the divergent wind. Over 90% of $\vec{\nabla}\cdot k\vec{V}_T$ is attributable to the divergent wind at 0600 GMT 25 April when the second MCC is near peak intensity. The rotational wind, on the other hand, generally provides a source of energy to the region. Flux convergence is prominent during the period between the two convective outbreaks and at the start of the experiment. Relatively weak flux divergence occurs at both peak convection times, while a strong sink is evident at the final time. Even though 36 h composite values (Table 4) indicated that $\vec{\nabla}\cdot k\vec{V}_D$ dominates the total flux, an examination of the individual times (Table 7) reveals that this dominance actually occurs only during the intense convective periods. Again, one should recall that K_D is much smaller than its nondivergent counterpart (Table 6).

Figure 7 shows pressure-time cross sections of $\vec{\nabla}\cdot k\vec{V}_D$ and $\vec{\nabla}\cdot k\vec{V}_R$. Energy export due to $\vec{V}_D$ is maximized within the 300-200 mb layer. Greatest values at this height occur at 0600 GMT 24 April (3.26 W m^{-2}/100 mb) and at 1200 GMT 25 April (3.96 W m^{-2}/100 mb). The diagram for rotational flux shows a less distinct pattern with greatest values near 300 mb at the last observation time.

The relative importance of the divergent wind during these convective outbreaks, which does not include a major cyclone, is similar to that noted by Chen et al. (1978) during a period of major cyclogensis. Important features of the two investigations include:

1) Term K_D is nearly two orders of magnitude smaller than K_R in both cases. Global studies by Chen and Wiin-Nielson (1976) also found small values of K_D/K_T, and as observed here, maximum values of K_D were found near jet stream level.

2) Term $\vec{V}\cdot k\vec{V}_D$ accounts for a significant percentage of the total horizontal flux. In the cyclone study, 25 - 50% of $\vec{V}\cdot k\vec{V}_T$ was due to the divergent wind. In the present case, as much as 90% of the total horizontal flux is attributable to $\vec{V}_D$ during times of peak convection.

3) In both studies, rotational generation generally is negative and opposes positive contributions by the divergent component. During the cyclone case, divergent generation was a maximum when the cyclone was most intense. During AVE 4, this maximum is not evident during the first convective outbreak, but is observed during the second MCC.

4) Both components produced flux convergence at all levels in the cyclone case, but opposing contributions are observed during AVE 4. This could be due to differing locations and strengths of the jet streams with respect to the computational areas.

5) An important conclusion is that K_D is as important during the severe storm outbreaks as during the extratropical cyclone case.

c. Spatial distribution of energy budget terms

Roles of the divergent and rotational wind components have been discussed within the context of the entire computational region. However, averaging over such a large area does not permit a detailed study of relationships between the energy budget terms and the enclosed convection. Therefore, spatial maps of selected budget terms will be presented to further explore interactions between the storms and their surrounding synoptic-scale environments. Horizontal fields of the divergent and rotational components of kinetic energy content, generation, and horizontal flux are presented during the life cycle of the second MCC (0000 GMT to 1200 GMT 25 April). Fields describing the surface-700 mb layer are denoted as layer 1, while maps for the upper troposphere (400-100 mb) are denoted as layer 3. Corresponding maps of the total kinetic energy budget have been presented by Fuelberg and Scoggins (1978). It should again be stressed that energetics of the synoptic-scale storm environments are being investigated, not the individual convective elements.

1) Kinetic energy

Spatial maps of divergent kinetic energy content are given in Figs. 8 and 9 for the lower and upper troposphere, respectively. At 0000 GMT, weak values of K_D are found in both

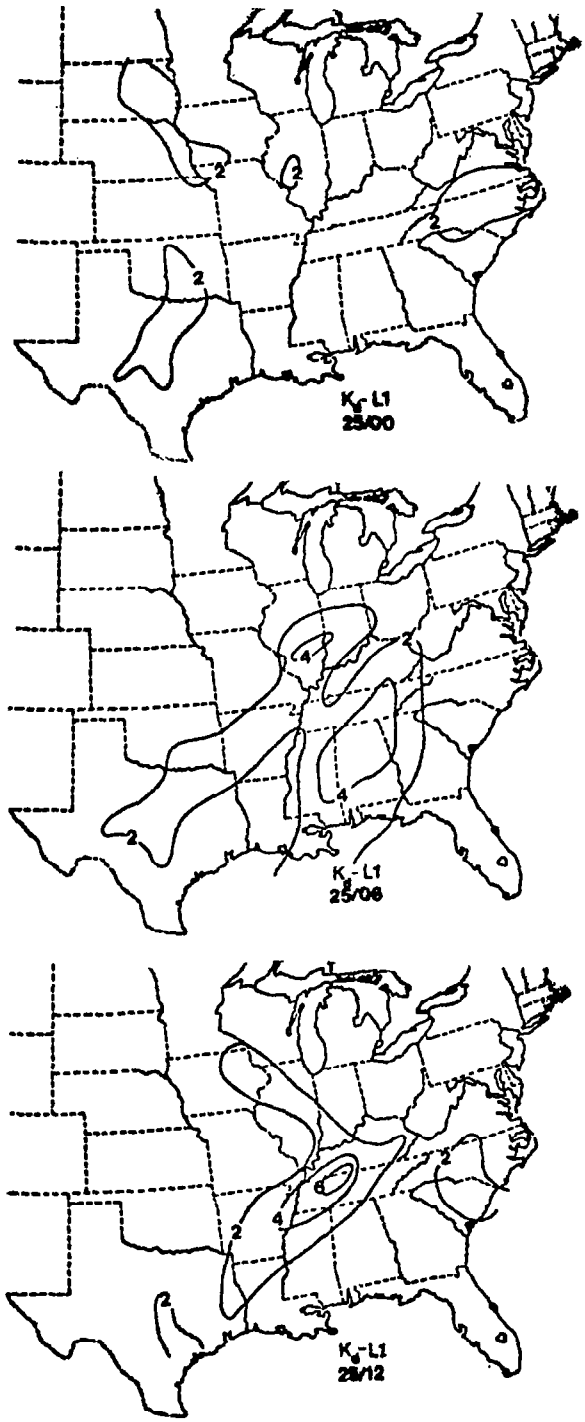

Fig. 8. Horizontal maps of term K_{D_4} within the surface-700 mb layer (L1). Values are 10^4 J m^{-2}.

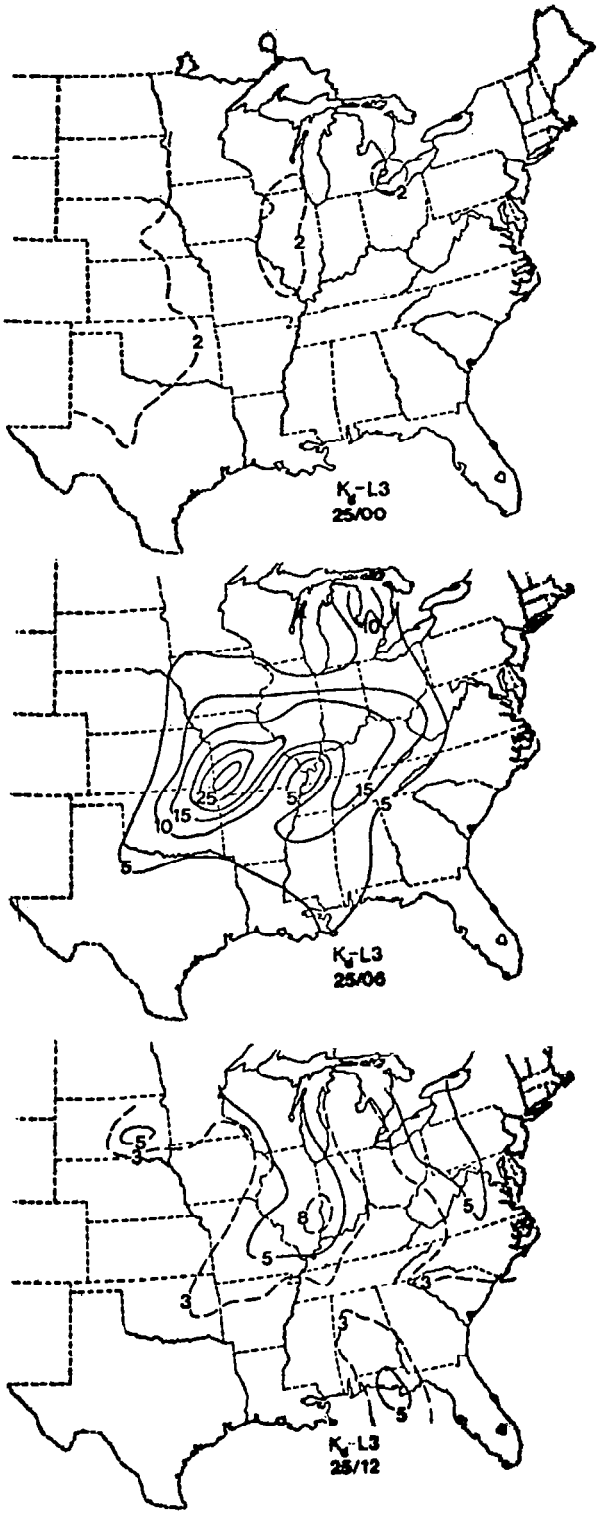

Fig. 9. Horizontal maps of term K_{D_4} within the 400-100 mb layer (L3). Values are 10^4 J m^{-2}.

layers. By 0600 GMT, however, two areas of maximum K_D can be seen in the lower troposphere. The western region, extending from Indiana to central Texas, agrees favorably with the locations of strongest convective activity (Fig. 5). The second area, over the Tennessee River Valley, is found in advance of the convection and it contains a broad maximum with values greater than 4×10^4 J m^{-2}. In the upper troposphere (Fig. 9), values of K_D increase greatly between 0000 GMT and 0600 GMT. A well defined maximum greater than 25×10^4 J m^{-2} is located over Missouri, just northwest of the MCC. This region of strongest K_D is near the greatest upper-level velocity divergence; at 200 mb values reach 14×10^{-5} s^{-1}. At 1200 GMT, as the convection decreases in intensity, the field of K_D in the lower troposphere (Fig. 8) appears more organized and closely related to storm locations. Maximum values over western Tennessee are located very near the tallest echo tops (Fig. 5). In the upper troposphere (Fig. 9), K_D has decreased dramatically between 0600 GMT and 1200 GMT. Maximum values now are located over Illinois and Indiana, northwest of the weakening MCC.

Since the rotational wind comprises a great proportion of the total flow, fields of K_R (Figs. 10 and 11) closely resemble those of K_T (not shown). At 0000 GMT, K_R in the lower levels is maximized along a band extending from the East Coast to the western Gulf of Mexico (Fig. 10). In the upper troposphere at 0000 GMT (Fig. 11), large values of K_R extend from Texas to the

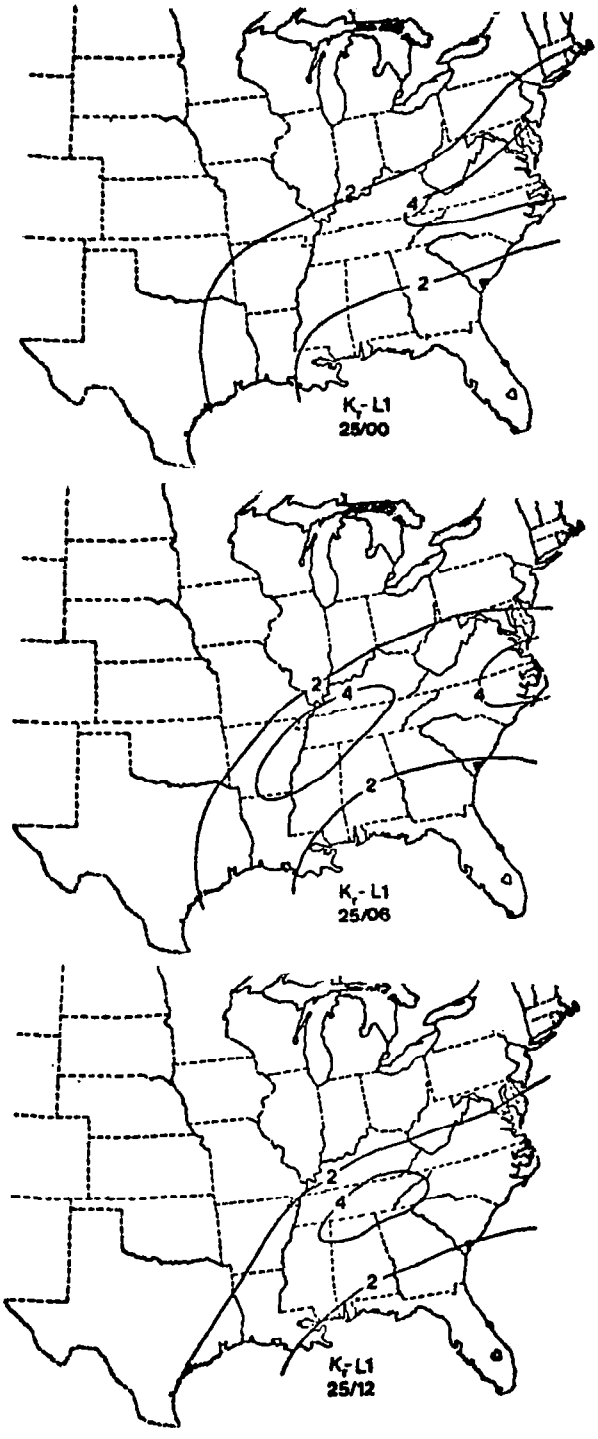

Fig. 10. Horizontal maps of term K_R within the surface-700 mb layer (L1). Values are 10^5 J m^{-2}.

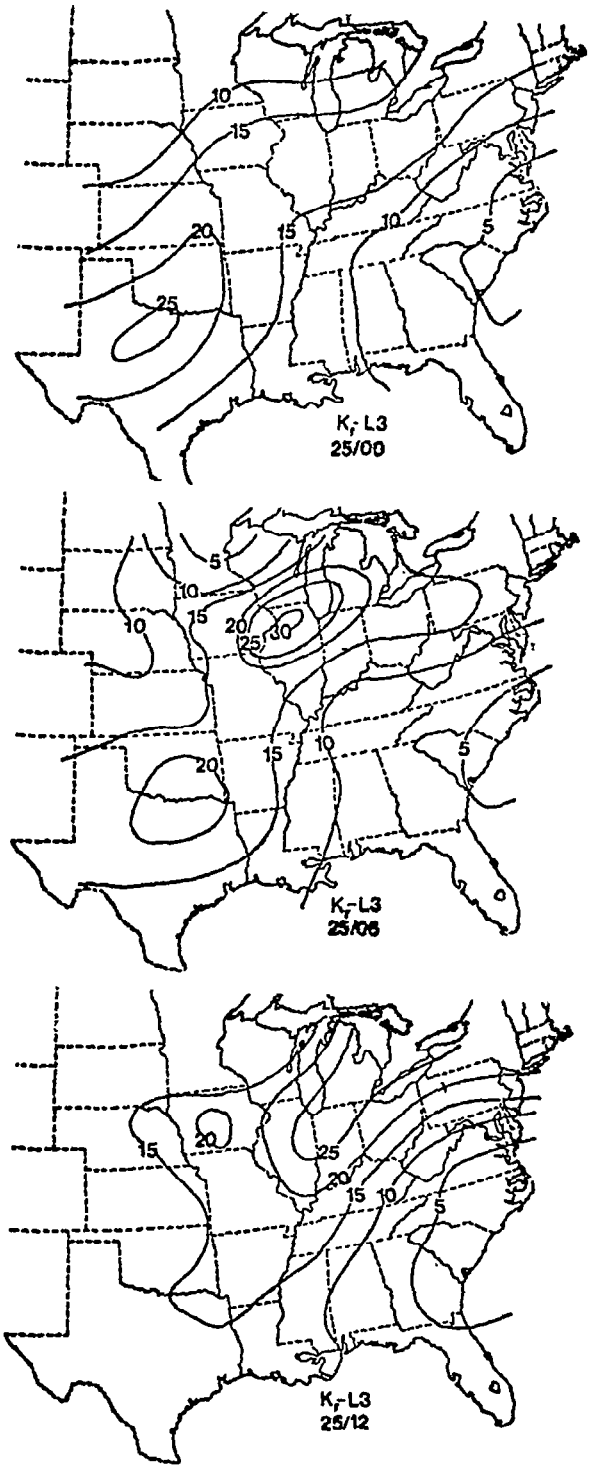

Fig. 11. Horizontal maps of term K_{R_5} within the 400-100 mb layer (L3). Values are 10^5 J m^{-2}.

eastern Great Lakes. Maximum values are located over northern Texas. The developing convection, is occurring just in advance of the K_R maximum (Fig. 5). By 0600 GMT (Fig. 10), a new maximum of K_R forms in the lower troposphere along the eastern edge of the now intense complex. This maximum persists and remains along and east of the strongest thunderstorms through 1200 GMT. In the upper troposphere at 0600 GMT (Fig. 11), a new K_R maximum has developed suddenly. Values greater than 30 x 10^5 J m^{-2} are located over northern Illinois, immediately north of the convective complex. A weaker, secondary maximum continues over northern Texas and Oklahoma. By 1200 GMT, strongest K_R is located in the upper Ohio River Valley, well behind the MCC. The formation of upper-level wind maxima north of MCC's appears to be a common feature of these organized convective systems (Fritsch and Maddox, 1981a). Explanations for such development will be sought in following sections.

2) Generation of kinetic energy

Figures 12 and 13 show the spatial distribution of cross-contour generation by the divergent wind. At 0000 GMT, values of $\vec{V}_D \cdot \vec{\nabla}\phi$ are weak in both the upper and lower troposphere. By 0600 GMT, the lower troposphere contains destruction of energy near the intense convection while generation is evident to the east of the complex. This pattern continues through 1200 GMT. In the upper troposphere (Fig. 13), startling changes occur

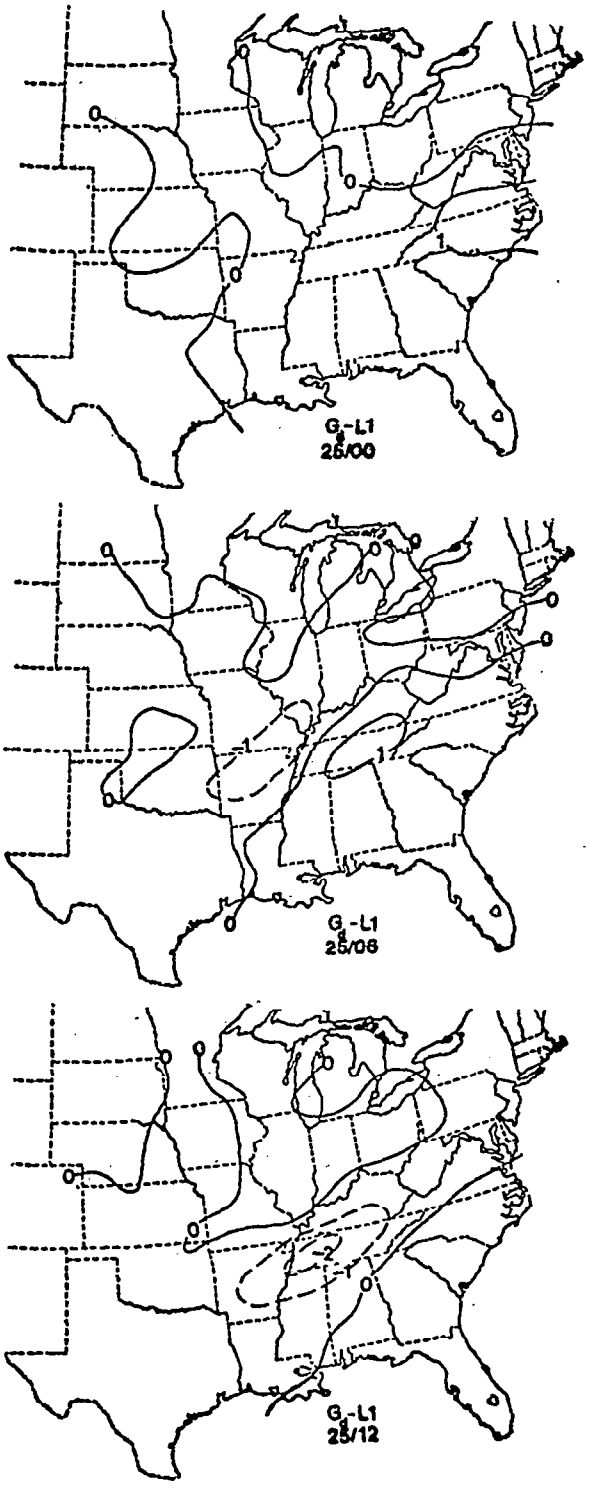

Fig. 12. Horizontal maps of term $-\vec{V}_D \cdot \vec{\nabla}\phi$ (G_d) within the surface-700 mb layer (L1). Values are in W m^{-2}.

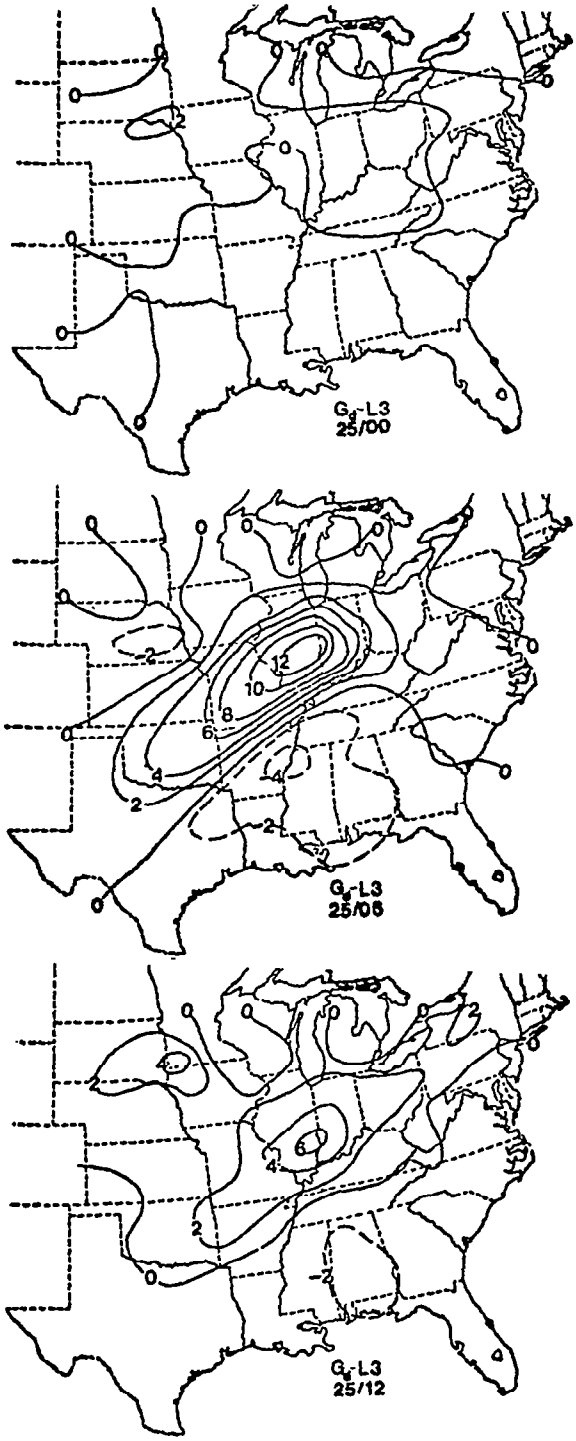

Fig. 13. Horizontal maps of term $-\vec{V}_D \cdot \vec{\nabla}\phi$ (G_d) within the 400-100 mb layer (L3). Values are in 10^1 W m^{-2}.

between 0000-0600 GMT. Very strong generation of kinetic energy develops immediately northwest of the severe thunderstorms. Weaker destruction is evident south and east of the MCC. The intensity of the generation (greater than 120 W m^{-2}) can be attributed to thunderstorm induced outflow being directed poleward across the height contours toward lower values. Magnitudes of $\vec{V}_D$ at 200 mb are as great as 14 m s^{-1} in this region. One should note that the area of greatest generation is located near the region of strong K_R increases (Fig. 9). By 1200 GMT, strong generation of energy continues northwest of the complex; however, the intensity has decreased significantly.

Generation by the rotational wind in the lower troposphere is shown in Fig. 14. Values are weak at 0000 GMT, but by 0600 GMT an area of strong generation develops over western Tennessee and remains nearly stationary through 1200 GMT. Destruction of energy over the southern Appalachians at 0600 GMT decreases in intensity by 1200 GMT. In the upper troposphere (Fig. 15), regions of strong generation and destruction cover much of the AVE 4 region. At 0000 GMT, generation by $\vec{V}_R$ clearly dominates that due to $\vec{V}_D$ (Figs. 13 and 15); however, by 0600 GMT, generation by the two wind components is of equal importance. An especially interesting feature at 0600 GMT is a couplet of strong generation and destruction over the upper Mississippi and Ohio River Valleys. Upper-level anticyclonic flow in the vicinity of the storms is the apparent cause for this pattern. Fritsch and Maddox (1981a) have noted anticyclonic flow near jet stream

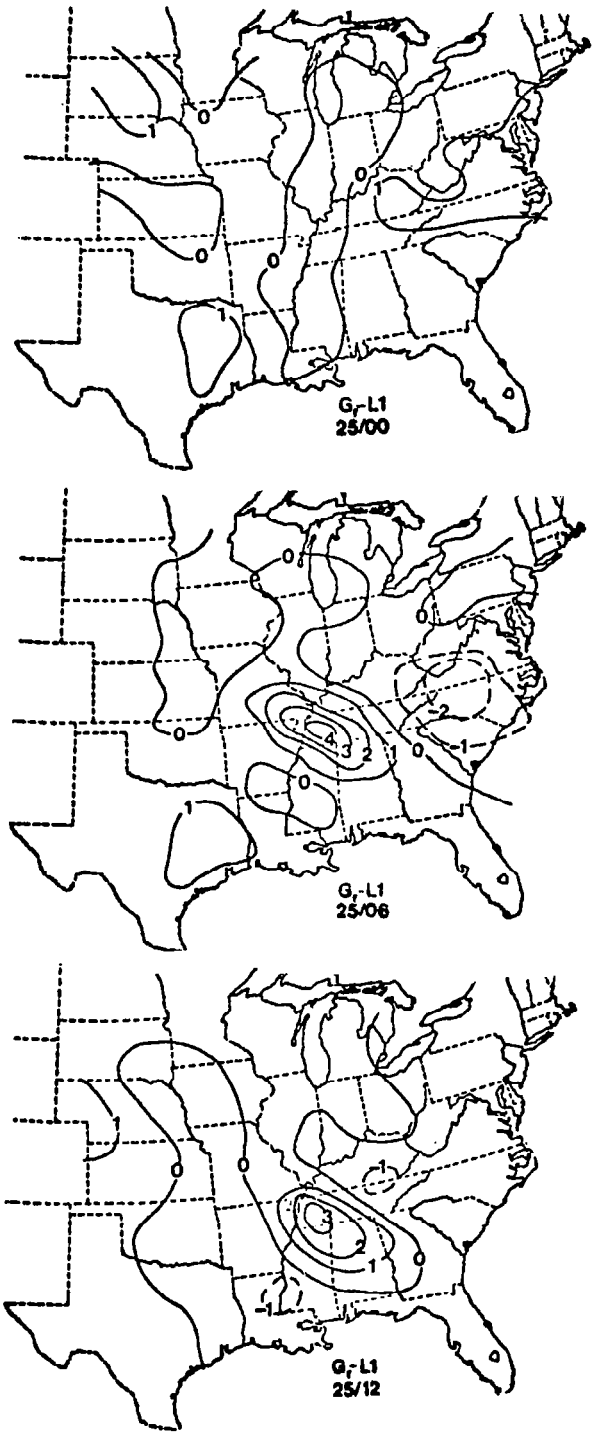

Fig. 14. Horizontal maps of term $-\vec{V}_R \cdot \vec{\nabla}\phi$ (G_r) within the surface-700 mb layer (L1). Values are in W m^{-2}.

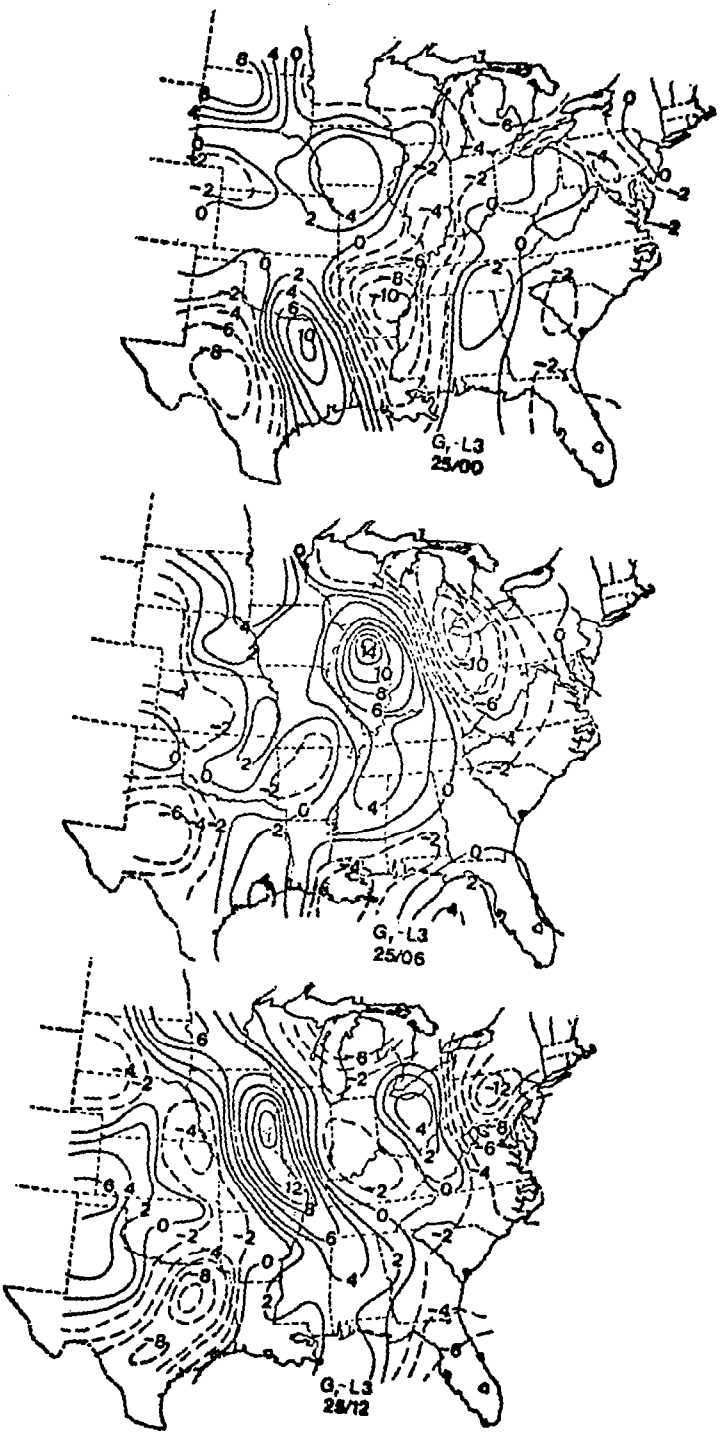

Fig. 15. Horizontal maps of term $-\vec{V}_R \cdot \vec{\nabla}\phi$ (G_r) within the 400-100 mb layer (L3). Values are in 10^1 W m^{-2}.

levels of numerous MCC's. Strong generation by both components produces a total value greater than 200 W m^{-2} over Illinois, near the region of strong K_R increases (Fig. 9). Generation by $\vec{V}_R$ persists over the upper Mississippi River Valley through 1200 GMT; however, the area of destruction to the east decreases in intensity (Fig. 15).

3) Horizontal flux of kinetic energy

In the lower troposphere, flux convergence of energy due to $\vec{V}_D$ occurs along and east of the MCC throughout its life cycle (Fig. 16). At peak storm intensity (0600 GMT) maximum flux convergence is located over Arkansas, southeast of the strongest thunderstorms (Fig. 5). This area moves northeastward by 1200 GMT as does the strongest convection. Flux divergence is found to the rear of the convective complex at all three times. The upper troposphere is characterized by weak values of $\vec{\nabla}\cdot k\vec{V}_D$ at 0000 GMT (Fig. 17). Flux convergence occurs over northern Indiana while weak flux divergence is found over the developing storm complex. Spectacular increases occur by 0600 GMT when very strong flux divergence develops over the entire convective complex. The maximum, containing values greater than 140 W m^{-2} over southern Illinois, is near the region of greatest upper-level velocity divergence (not shown). Strong flux convergence of energy has developed over northern Illinois, downwind of the developing K_T maximum. One should recall that K_R approximates

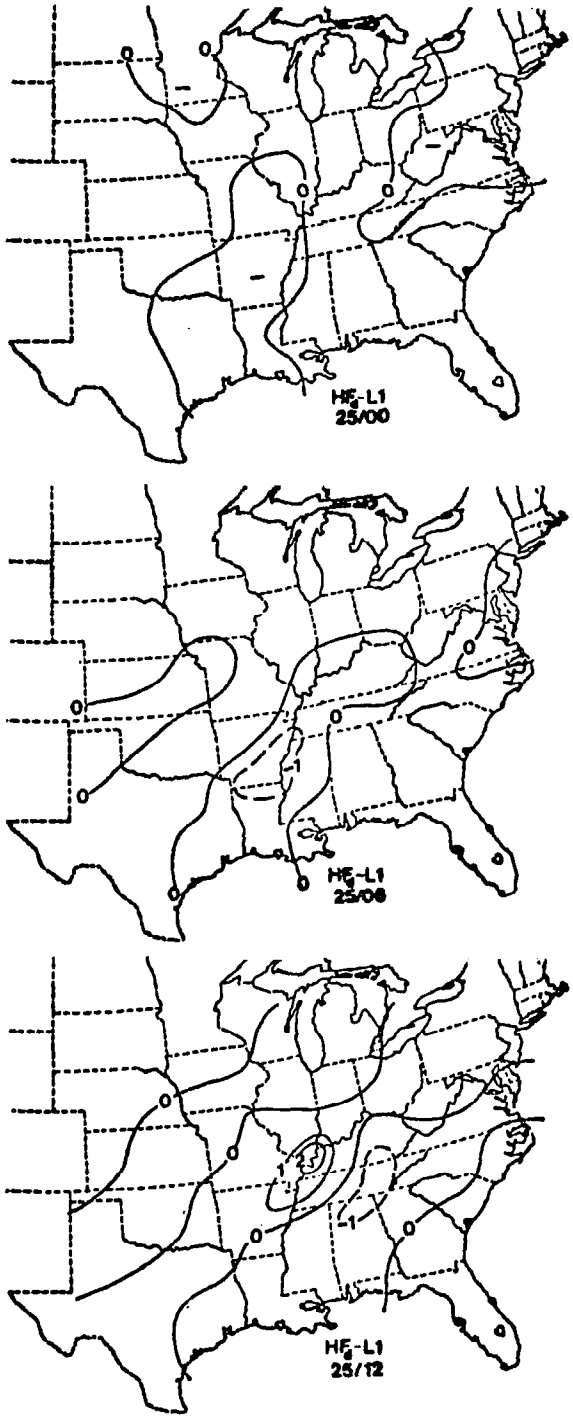

Fig. 16. Horizontal maps of term $\vec{\nabla}\cdot k\vec{V}_D$ (HF_d) within the surface-700 mb layer (L1). Values are in W m^{-2}.

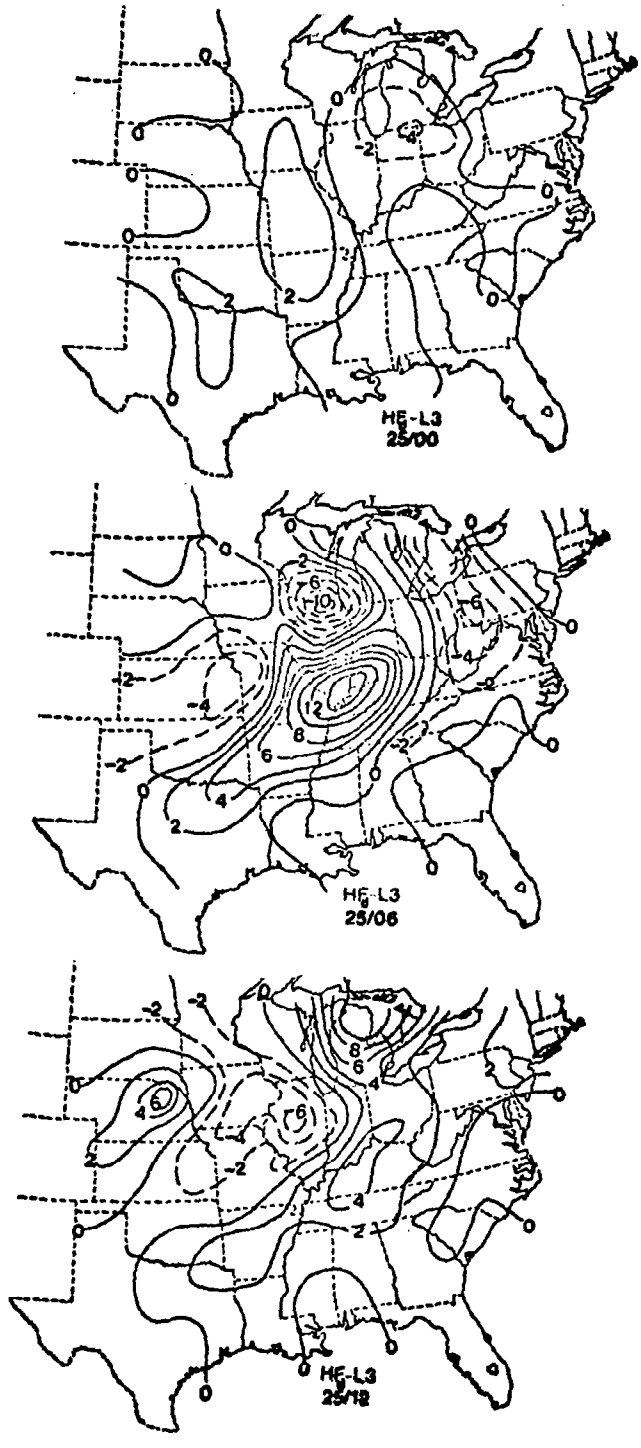

Fig. 17. Horizontal maps of term $\vec{\nabla}\cdot k\vec{V}_D$ (HF_d) within the 400-100 mb layer (L3). Values are in 10^1 W m^{-2}.

K_T; therefore, the K_T pattern is similar to that of Fig. 11. At 1200 GMT (Fig. 17), flux divergence continues over the weakening convection although values have decreased. The flux convergence over Illinois also has weakened.

Horizontal maps of $\vec{\nabla}\cdot k\vec{V}_R$ are given in Figs. 18 and 19. These fields reflect the advection of K_T patterns since the $k\vec{\nabla}\cdot\vec{V}_R$ component of the flux term is near zero. Flux convergence generally is located east of the MCC while flux divergence occurs behind the storms. Greatest magnitudes are observed at the last observation time. In the upper troposphere at 0000 GMT (Fig. 19), values of $\vec{\nabla}\cdot k\vec{V}_R$ are weak. By 0600 GMT, however, a strong center of flux divergence is located over the upper Mississippi River Valley, north of the convective complex and upwind of the K_T maximum that is approximated by Fig. 11. Peak values of 280 W m^{-2} are nearly twice those of $\vec{\nabla}\cdot k\vec{V}_D$ (Fig. 17); however, the two maxima are not co-located and the area due to $\vec{V}_R$ is considerably smaller. Weaker flux convergence is located over northern Illinois and eastward. At 1200 GMT weak flux convergence is occurring over the convective complex that stretches from the Appalachians to Arkansas (Fig. 5). Maximum flux divergence is located over the Great Lakes, behind the wind maximum that is exiting the region.

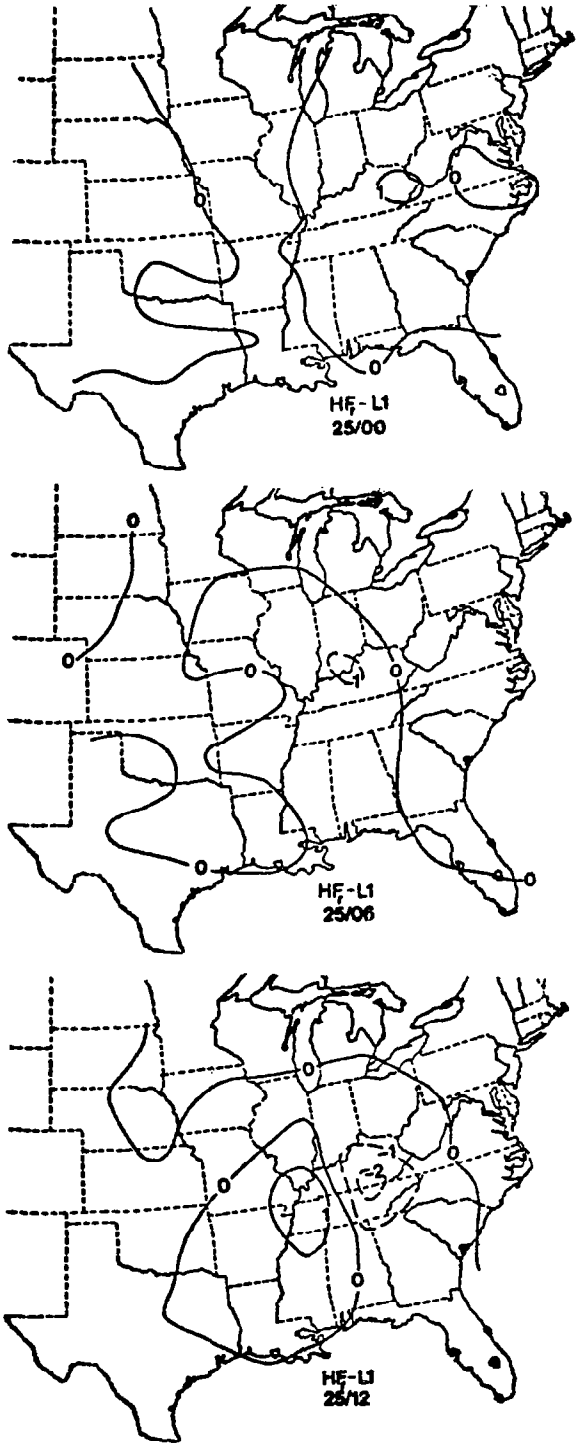

Fig. 18. Horizontal maps of term $\vec{\nabla}\cdot k\vec{V}_R$ (HF_r) within the surface-700 mb layer (L1). Values are in W m^{-2}.

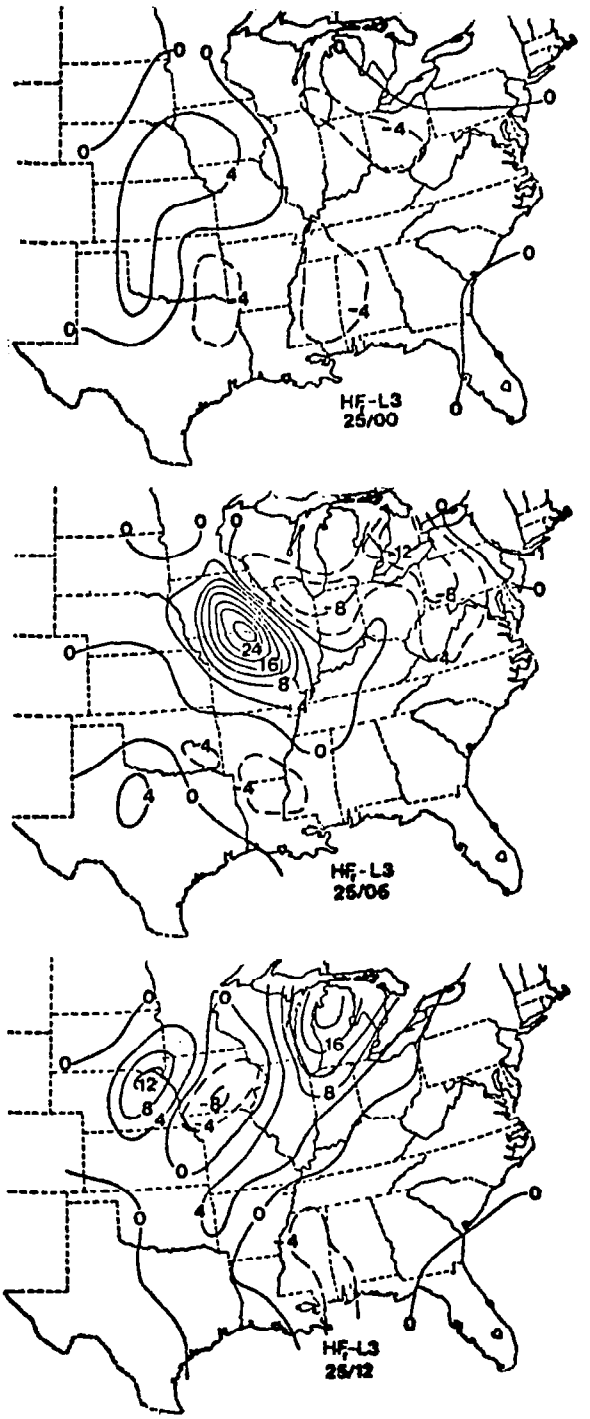

Fig. 19. Horizontal maps of term $\vec{\nabla}\cdot k\vec{V}_R$ (HF_r) within the 400-100 mb layer (L3). Values are in 10^1 W m^{-2}.

d. Energy budgets of convection subregions

To quantify energetics of the near storm environment, energy budgets were obtained for subvolumes of the total region that just enclosed the convective areas. These volumes, based only on MDR data (Table 1), moved with the convection and were identical to those used by Fuelberg and Scoggins (1978). Although the limited areas were only about one-fourth the total computational region, it should be emphasized that their budgets describe energetics of the synoptic-scale flow in which the convection was embedded, and not the individual storms themselves. Figure 20 is an example of the boundaries and associated MDR coding for 0600 GMT 25 April. The average area of these smaller subregions was 10^{12} m^2.

Time variability of the total flow energy terms is shown in Table 8 for the second MCC (MCC2). Total kinetic energy increases to a peak value of 27.3 x 10^5 J m^{-2} at 0000 GMT, then decreases with time through 1200 GMT. Generation due to cross-contour flow provides an energy source throughout the MCC's life cycle with a maximum value occurring near peak storm intensity (0600 GMT). Flux divergence and negative dissipation are responsible for the decreases in K_T after 0000 GMT. Although flux divergence of energy out of the region occurs at every time after 1800 GMT, the maximum value of 43.9 W m^{-2} is observed during greatest convective activity. Transfer of energy to subgrid scales of motion occurs at each time. As noted by Fuelberg and Scoggins

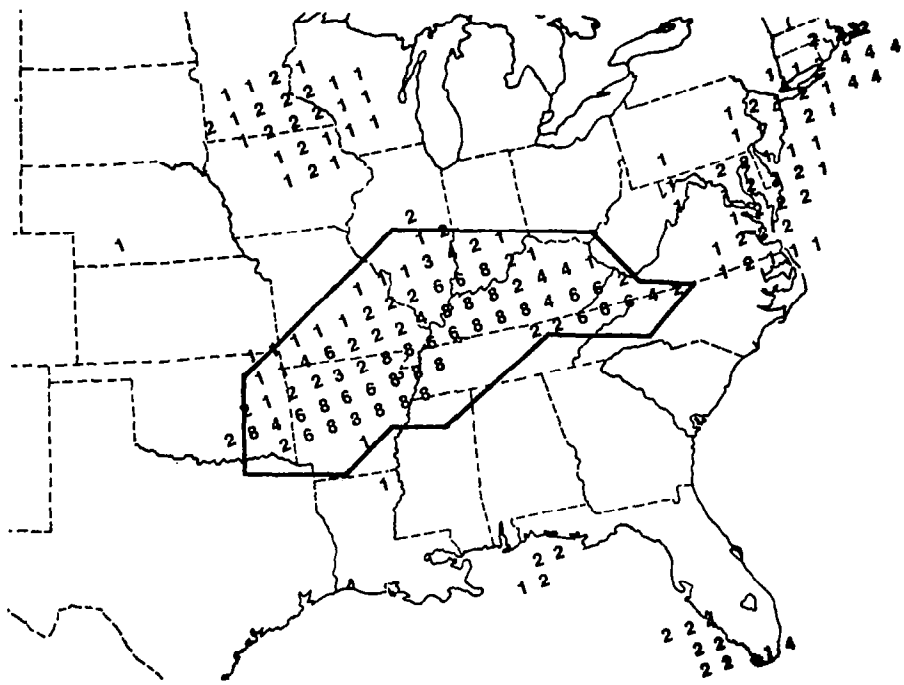

Fig. 20. Example of the limited volume used to enclose the convection at 0600 GMT 25 April. The area enclosed is 12.2×10^{11} m^2.

Table 8. Vertical totals of the kinetic energy budget for limited volumes enclosing MCC2 at individual observation times. All units are W m^{-2} except K_T which is 10^5 J m^{-2}.

Date/Time	K_T	$\partial K_T/\partial t$	$-\vec{V}_T \cdot \vec{\nabla}\phi$	$\vec{\nabla} \cdot k\vec{V}_T$	D
24/18	24.7	6.0	7.4	-21.5	-22.9
24/21	25.8	5.1	19.5	11.6	- 2.8
25/00	27.3	-12.0	4.6	13.0	- 3.6
25/06	25.5	- 6.3	52.2	43.9	-14.6
25/12	23.8	- 7.9	21.1	10.3	-18.7
Composite	25.4	- 3.0	21.0	11.5	-12.5

(1978), these major energy conversions and transports near the convective complex are in striking contrast to the much weaker processes observed for the AVE 4 experiment area as a whole (Table 2).

Table 9 gives components of kinetic energy content for MCC2. Values of K_D show a cyclic variation that is closely related to the life cycle of the convection. Magnitudes increase nearly five-fold between 0000-0600 GMT as the storms intensify, and then decrease between 0600-1200 GMT as the storms weaken. At 0600 GMT, the value of 1.72×10^5 J m^{-2} constitutes 6.7% of the total kinetic energy content. It is noteworthy that terms K_T and K_R decrease between 0000-0600 GMT. However, one should recall that a maximum of K_R did form north of the storm area (Fig. 11) - outside of the limited region (Fig. 20). Thus, placement of the limited volume is quite important. Values of $\vec{V}_R \cdot \vec{V}_D$ remain negative during the MCC's life cycle, and are smallest at the time of peak convection.

Generation of kinetic energy by the total flow increases from 4.6 W m^{-2} at 0000 GMT to 52.2 W m^{-2} only 6 h later at peak storm intensity (Table 10). Although both wind components blow toward lower heights and thereby generate kinetic energy at 0600 GMT, the divergent component is the primary contributor to the sudden increase within the limited region. Even though K_D is a small fraction of the total kinetic energy content (Table 9), divergent generation (35.7 W m^{-2}) accounts for 68% of

Table 9. Vertical totals of the components of kinetic energy content for limited volumes enclosing MCC2 at individual observation times. Units of energy are 10^5 J m^{-2}.

Date/Time	K_T	K_R	K_D	$\vec{V}_R \cdot \vec{V}_D$	K_D/K_T
24/18	24.7	26.3	0.33	-1.9	1.3%
24/21	25.8	27.4	0.38	-2.0	1.5%
25/00	27.3	27.6	0.37	-0.7	1.4%
25/06	25.5	24.0	1.72	0.2	6.7%
25/12	23.8	23.7	0.63	-0.5	2.6%
Composite	25.4	25.8	0.69	-1.1	2.7%

Table 10. Vertical totals of the components of generation and horizontal flux divergence for limited volumes enclosing MCC2 at individual observation times. All units are W m^{-2}.

Date/Time	$-\vec{V}_T \cdot \vec{\nabla}\phi$	$-\vec{V}_R \cdot \vec{\nabla}\phi$	$-\vec{V}_D \cdot \vec{\nabla}\phi$	$\vec{\nabla} \cdot k\vec{V}_T$	$\vec{\nabla} \cdot k\vec{V}_R$	$\vec{\nabla} \cdot k\vec{V}_D$
24/18	7.4	- 6.2	13.6	-21.5	-20.3	- 1.2
24/21	19.5	18.3	1.2	11.6	- 0.7	12.3
25/00	4.6	7.9	- 3.3	13.0	1.1	11.9
25/06	52.2	16.5	35.7	43.9	5.6	38.3
25/12	21.1	14.5	6.6	10.3	- 2.5	12.8
Composite	21.0	10.2	10.8	11.5	- 3.3	14.8

$-\vec{V}_T \cdot \vec{\nabla}\phi$. Generation decreases after 0600 GMT as the storms weaken.

Horizontal flux divergence provides a major energy sink to the storm region, especially when the storms are most intense (Table 10). The divergent wind component is the major cause for this export. After 1800 GMT, values of $\vec{\nabla}\cdot k\vec{V}_D$ are consistently positive and greater in magnitude than those of $\vec{\nabla}\cdot k\vec{V}_R$. As observed with previous terms involving the divergent component, a major increase in $\vec{\nabla}\cdot k\vec{V}_D$ occurs between 0000-0600 GMT. At 0600 GMT, the divergent wind contributes 38.3 W m^{-2} or 87% of the total flux divergence within the limited volume. The influence of $\vec{V}_R$ is much greater to the northwest of the storm region (Figs. 17 and 19).

It is informative to describe vertical variations of the energy terms within the subvolume at peak storm intensity (0600 GMT 25 April). Vertical distributions of total flow energy terms are given in Table 11. Maximum kinetic energy content occurs at jet stream level (300-200 mb layer). Values are considerably greater than those of the composite area-time average (Table 2). Generation of kinetic energy due to cross-contour flow is a source at nearly all levels; however, greatest values are found in the upper troposphere. Horizontal flux divergence is a major exporter of energy above 500 mb, with a maximum of 28.8 W m^{-2}/100 mb at jet level. Below 500 mb, weak horizontal flux convergence occurs. The vertical flux term

Table 11. Average kinetic energy budget for the limited area enclosing the convection at 0600 GMT 25 April. All units are W m^{-2} except K_T which is 10^5 J m^{-2}.

Pressure Layer (mb)	K_T	$\partial K_T/\partial t$	$-\vec{V}_T \cdot \vec{\nabla}\phi$	$\vec{\nabla} \cdot k\vec{V}_T$	$\partial \omega k/\partial p$	D
200-100	4.8	-2.2	4.3	7.5	- 4.8	- 3.8
300-200	6.0	0.2	16.9	28.8	-11.6	0.5
400-300	4.4	-0.1	14.3	10.8	- 6.5	-10.1
500-400	3.6	-1.4	11.0	1.3	2.7	- 8.4
600-500	2.6	-0.9	4.1	- 0.9	7.3	1.4
700-600	1.7	-1.0	0.5	- 1.2	8.1	5.4
800-700	1.0	-0.5	-2.6	- 0.3	2.5	4.3
900-800	0.9	-0.3	1.3	- 1.1	1.2	- 1.5
SFC-900	0.5	-0.1	2.4	- 1.0	1.1	- 2.4
Vertical Total	25.5	-6.3	52.2	43.9	0.0	-14.6

$\partial\omega k/\partial p$ indicates strong upward transport because values of synoptic-scale vertical motion near the storm complex are as great as -16 $\mu b\ s^{-1}$ at 500 mb. Transfers of energy to subgrid scales provide an important energy sink at 0600 GMT. Destruction below 800 mb is due to surface friction; negative values also occur in the upper troposphere. Transfer of energy from subgrid to resolvable scales of motion (positive dissipation) is observed between 800-500 mb and within the 300-200 mb layer. Middle tropospheric positive dissipation also has been observed in convective storm environments by Vincent and Schlatter (1979).

Vertical distributions of kinetic energy content at 0600 GMT, shown in Table 12, show the importance of $\vec{V}_D$ near jet level. Within the 300-200 mb layer, where velocity divergence reaches 14 x 10^{-5} s^{-1}, the divergent wind component provides an 11.8% contribution to K_T. An additional maximum of K_D, occurring in the 700-800 mb layer, comprises 12% of K_T and is due to the pronounced low-level velocity convergence in the storm environment. The vertical distribution of K_R closely follows that of K_T with a maximum value at jet level. Thus, failure to include $\vec{V}_D$ in analyses of the storm region would produce energy errors ranging between 2-12% within individual 100 mb layers.

Generation of kinetic energy as a function of pressure is shown in Fig. 21 and Table 13. Except for the 200-100 mb layer, the rotational component creates kinetic energy at all levels; maximum generation occurs near 350 mb. Within the storm volume,

Table 12. Components of average kinetic energy content for the limited area enclosing the convection at 0600 GMT 25 April. Units of energy are 10^5 J m^{-2}.

Pressure Layer (mb)	K_T	K_R	K_D	$\vec{V}_R \cdot \vec{V}_D$	K_D/K_T
200-100	4.8	4.5	0.22	0.12	4.6%
300-200	6.0	5.4	0.71	-0.10	11.8%
400-300	4.4	4.0	0.32	0.08	7.3%
500-400	3.6	3.3	0.11	0.16	3.1%
600-500	2.6	2.5	0.06	0.05	2.3%
700-600	1.7	1.7	0.08	-0.11	4.7%
800-700	1.0	1.2	0.12	-0.29	12.0%
900-800	0.9	1.0	0.07	-0.15	7.8%
SFC-900	0.5	0.4	0.03	0.03	6.0%
Vertical Total	25.5	24.0	1.72	-0.21	6.7%

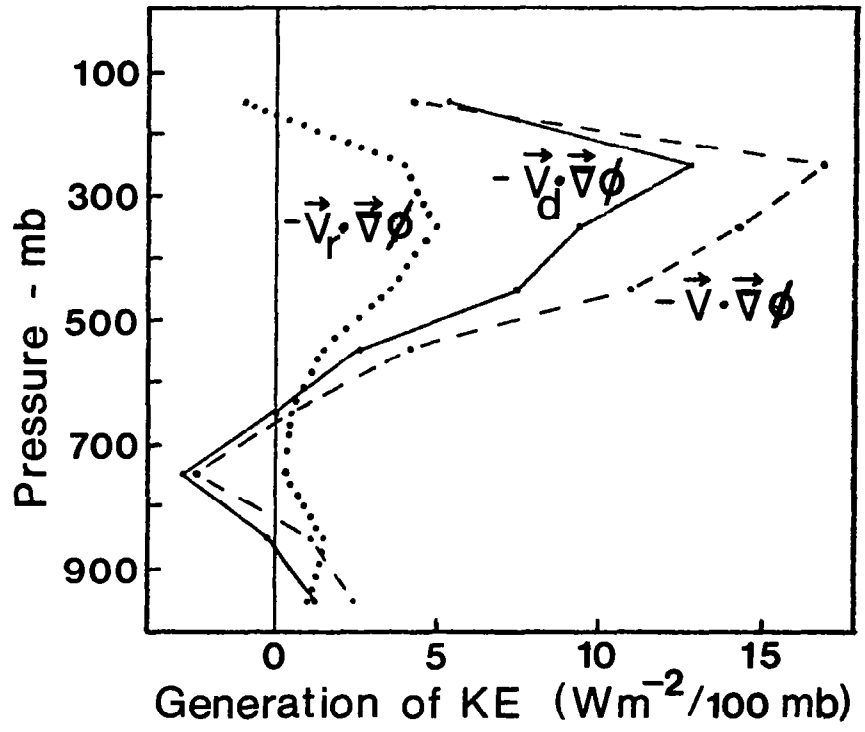

Fig. 21. Generation of kinetic energy in the limited volume enclosing the convection at 0600 GMT 25 April. All units are W m^{-2}/100 mb.

Table 13. Components of average generation and horizontal flux divergence for the limited area enclosing the convection at 0600 GMT 25 April. All units are W m^{-2}.

Pressure Layer (mb)	$-\vec{V}_T \cdot \vec{\nabla}\phi$	$-\vec{V}_R \cdot \vec{\nabla}\phi$	$-\vec{V}_D \cdot \vec{\nabla}\phi$	$\vec{\nabla} \cdot k\vec{V}_T$	$\vec{\nabla} \cdot k\vec{V}_R$	$\vec{\nabla} \cdot k\vec{V}_D$
200-100	4.3	-1.0	5.3	7.5	-1.0	8.5
300-200	16.9	4.1	12.8	28.8	3.8	25.0
400-300	14.3	5.0	9.3	10.8	2.2	8.6
500-400	11.0	3.5	7.5	1.3	0.7	0.6
600-500	4.1	1.5	2.6	- 0.9	0.3	- 1.2
700-600	0.5	0.5	0.0	- 1.2	0.3	- 1.5
800-700	- 2.6	0.3	- 2.9	- 0.3	0.2	- 0.5
900-800	1.3	1.5	- 0.2	- 1.1	-0.5	- 0.6
SFC-900	2.4	1.1	1.3	- 1.0	-0.4	- 0.6
Vertical Total	52.2	16.5	35.7	43.9	5.6	38.3

the divergent component provides a much stronger energy source above 500 mb than does the rotational component. Within these layers, over 75% of $-\vec{V}_T \cdot \vec{\nabla}\phi$ is due to $\vec{V}_D$. Near 750 mb, however, $\vec{V}_D$ predominantly crosses the contours toward higher values, thereby destroying kinetic energy. Since generation by the divergent wind greatly exceeds that due to the nondivergent wind, the profile for total generation is similar to that of $-\vec{V}_D \cdot \vec{\nabla}\phi$ (Fig. 21).

Vertical profiles of the horizontal flux terms at 0600 GMT (Fig. 22 and Table 13) show that greatest outflow from each component occurs near the jet stream level (250 mb); however, magnitudes from $\vec{V}_D$ far exceed those from $\vec{V}_R$. Within the 300-200 mb layer, nearly 87% of the total flux divergence is due to $\vec{V}_D$. Neither component produces large magnitudes in the lower and middle troposphere. These results indicate that failure to include $\vec{V}_D$ in computational work would produce serious misrepresentations of kinetic energy generation and transport within the storm environment.

To verify the role of the divergent wind during intense convective outbreaks, the energetics of the first MCC (MCC1) which occurred early in the AVE 4 experiment (0000-1500 GMT 24 April) are presented. Boundaries for the subvolumes that enclose it again are identical to those of Fuelberg and Scoggins (1978). One should note the numerous similarities between these two cases. Values of K_D for MCC1 (Table 14) show a cyclic variation which is similar to that observed for MCC2 (Table 9). A maximum

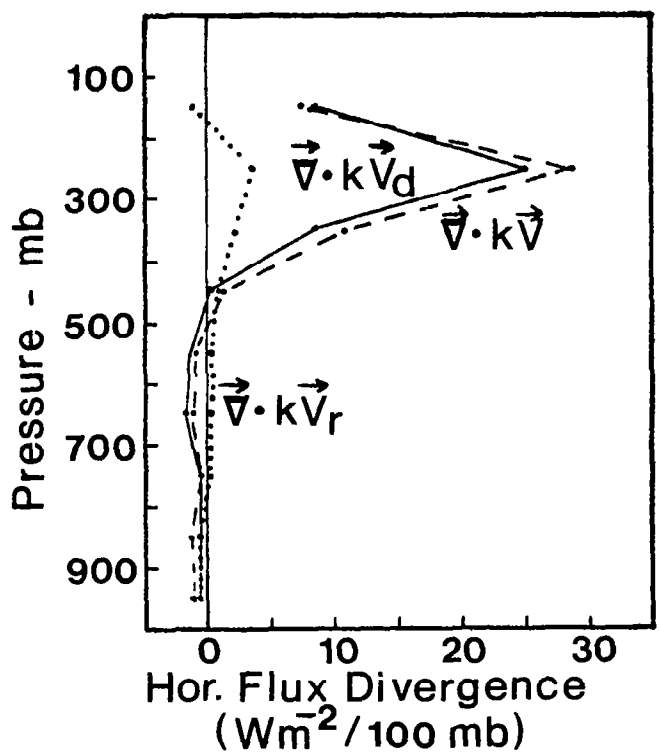

Fig. 22. Horizontal flux divergence of kinetic energy in the limited volume enclosing the convection at 0600 GMT 25 April. All units are W m^{-2}/100 mb.

Table 14. Vertical totals of the components of kinetic energy content for limited volumes enclosing MCC1 at individual observation times. Units of energy are 10^5 J m^{-2}.

Date/Time	K_T	K_R	K_D	$\vec{V}_R \cdot \vec{V}_D$	K_D/K_T
24/00	30.8	31.2	0.42	-0.8	1.4%
24/06	24.1	23.6	1.00	-0.5	4.1%
24/12	26.4	25.4	0.87	0.1	3.3%
24/15	25.2	25.5	0.36	-0.6	1.4%
Composite	26.6	26.4	0.66	-0.5	2.5%

value of 1 x 10^5 J m^{-2}, or 4.1% of K_T, is observed at peak storm intensity (0600 GMT 24 April). The value of K_D doubles between 0000-0600 GMT, then decreases after 0600 GMT as the storms weaken. As with MCC2, values of K_T and K_R decrease within the subvolume as the storms intensify; however, maxima of K_R and K_T again form north and outside of the storm volume.

Generation of kinetic energy by the total flow increases from 30.2 W m^{-2} at 0000 GMT to 47.5 W m^{-2} 6 h later, at peak storm intensity (Table 15). Contrary to results for MCC2 (Table 10), the increase is due mostly to variations in rotational generation. Actually, however, horizontal fields of $-\vec{V}_D \cdot \vec{\nabla}\phi$ in the 400-100 mb layer (not shown) indicate strong generation of kinetic energy to the north of MCC1 and destruction to the south. This pattern is similar to that observed with MCC2 (Fig. 13). Maximum values of 104 W m^{-2} also are comparable to those of MCC2 (Fig. 13). With MCC1, however, the greatest effect of $\vec{V}_D$ occurs outside the limited region, thus accounting for the comparitively small values of divergent generation in Table 15. Thus, some of the contrasts between the two systems are attributable to the relative locations of the subvolumes with respect to particular energy features. Both total and rotational generation decrease dramatically between 0600-1200 GMT as the storms weaken (Table 15). Spatial maps of divergent generation show that it too decreases after 0600 GMT.

As with MCC2, horizontal flux divergence provides a major energy sink during the life cycle of the first convective com-

Table 15. Vertical totals of the components of generation and horizontal flux divergence for limited volumes enclosing MCC1 at individual observation times. All units are W m^{-2}.

Date/Time	$-\vec{V}_T \cdot \vec{\nabla}\phi$	$-\vec{V}_R \cdot \vec{\nabla}\phi$	$-\vec{V}_D \cdot \vec{\nabla}\phi$	$\vec{\nabla} \cdot k\vec{V}_T$	$\vec{\nabla} \cdot k\vec{V}_R$	$\vec{\nabla} \cdot k\vec{V}_D$
24/00	30.2	15.5	14.7	- 1.2	0.3	- 1.5
24/06	47.5	40.2	7.3	44.7	19.7	25.0
24/12	11.0	2.2	8.8	28.4	7.8	20.6
24/15	17.3	9.9	7.4	8.7	- 1.7	10.4
Composite	26.5	17.0	9.5	20.1	6.5	13.6

plex (Table 15). Again, a significant increase in $\vec{\nabla}\cdot k\vec{V}_D$ occurs between 0000-0600 GMT 24 April as the complex develops. The nondivergent component also increases during this 6 h period, and both components contribute nearly equally to $\vec{\nabla}\cdot k\vec{V}_T$ during peak convective activity.

Vertical distributions of kinetic energy content at 0600 GMT 24 April (Table 16) show that both components exhibit maxima at jet stream level. Within the 300-200 mb layer, K_D for MCC1 is only one-third that of MCC2 (Table 12), although it still contributes 4.4% of K_T. Spatial maps of K_D for the upper troposphere (not shown) indicate maximum values occurring on the poleward side of the convection, similar to that found for MCC2 (Fig. 9). A secondary maximum is observed in the lower troposphere near 850 mb (Table 16).

Table 17 gives vertical distributions for the components of generation and horizontal flux at 0600 GMT 24 April. Maximum generation occurs in the upper troposphere above 300 mb and appears due to the nondivergent wind. Again, it should be noted that the generation maximum due to $\vec{V}_D$ occurs north of the subvolume and therefore does not prominently appear in the Table. Both wind components produce horizontal flux divergence of energy above 500 mb and flux convergence below 500 mb. Horizontal flux due to $\vec{V}_D$ dominates $\vec{\nabla}\cdot k\vec{V}_T$ at nearly every level during peak convective activity.

Table 16. Components of average kinetic energy content for the limited area enclosing the convection at 0600 GMT 24 April. Units of energy are 10^5 J m^{-2}.

Pressure Layer (mb)	K_T	K_R	K_D	$\vec{V}_R \cdot \vec{V}_D$	K_D/K_T
200-100	5.2	5.1	0.10	-0.04	1.9%
300-200	5.4	5.5	0.24	-0.30	4.4%
400-300	3.7	3.7	0.07	-0.07	1.9%
500-400	3.0	2.6	0.06	0.32	2.0%
600-500	2.4	2.1	0.07	0.27	2.9%
700-600	1.7	1.6	0.11	-0.01	6.5%
800-700	1.3	1.4	0.13	-0.19	10.0%
900-800	1.0	1.2	0.17	-0.34	17.0%
SFC-900	0.4	0.4	0.09	-0.12	22.5%
Vertical Total	24.1	23.6	1.0	-0.5	4.1%

Table 17. Components of average generation and horizontal flux divergence for the limited area enclosing the convection at 0600 GMT 24 April. All units are W m^{-2}.

Pressure Layer (mb)	$-\vec{V}_T \cdot \vec{\nabla}\phi$	$-\vec{V}_R \cdot \vec{\nabla}\phi$	$-\vec{V}_D \cdot \vec{\nabla}\phi$	$\vec{\nabla} \cdot k\vec{V}_T$	$\vec{\nabla} \cdot k\vec{V}_R$	$\vec{\nabla} \cdot k\vec{V}_D$
200-100	12.2	11.0	1.2	10.9	4.3	6.6
300-200	11.8	10.0	1.8	29.5	10.4	19.1
400-300	6.2	4.6	1.6	12.8	5.2	7.6
500-400	4.7	2.1	2.6	3.7	2.7	1.0
600-500	3.3	1.8	1.5	- 2.3	- 0.2	- 2.1
700-600	4.4	3.1	1.3	- 3.5	- 0.6	- 2.9
800-700	2.9	3.6	-0.7	- 3.2	- 1.2	- 2.0
900-800	0.5	2.6	-2.1	- 2.3	- 0.9	- 1.4
SFC-900	1.5	1.4	0.1	- 0.9	0.0	- 0.9
Vertical Total	47.5	40.2	7.3	44.7	19.7	25.0

The major point to note is that the energetics of MCC1 generally are similar to those of MCC2. The divergent wind component is very important in each case. These agreements lend credibility to the overall study.

6. SUMMARY AND CONCLUSIONS

Relative contributions of divergent and rotational wind components to the kinetic energy balance of two severe storm environments have been investigated. Synoptic-scale rawinsonde data at 3 or 6 h intervals were available from NASA's AVE 4 experiment. Energy budgets were obtained for the entire computational region and for subvolumes that barely enclosed and moved with the two convective complexes. This study was an extension of the total kinetic energy analysis of AVE 4 by Fuelberg and Scoggins (1978).

The divergent wind component was found to be very important in the synoptic-scale environments of the two mesoscale convective complexes. Although K_D usually comprised less than 10% of the total kinetic energy, $\vec{V}_D$ was a major cause for energy generation by cross-contour flow and for horizontal flux divergence. Within the subvolumes, as much as 68% of the total cross-contour generation and 87% of the total horizontal flux in the upper troposphere was due to $\vec{V}_D$ during peak convective periods. The time variability of divergent energy transformations displayed a close correlation to the intensity of the convection. Pressure-time cross sections of K_D, $-\vec{V}_D \cdot \vec{\nabla}\phi$, and $\vec{\nabla} \cdot k\vec{V}_D$ each have indicated distinct maxima at times of peak convection. Since strong synoptic-scale, upper-level divergence may be a common by-product of certain types of storm regions (Fritsch and Maddox, 1981a and b), the importance of $\vec{V}_D$ during AVE 4 may be

characteristic of other cases as well. A comparison of current results with those from a period of cyclogenesis (Chen et al., 1978) suggests that $\vec{V}_D$ in major convective areas may affect the general circulation as much or more per unit area than in mature cyclone situations.

Generation of kinetic energy by the divergent component appears to have been a major factor leading to the creation of upper-level wind maxima north of the storm areas. Recent investigations suggest that similar wind perturbations are common occurrences near certain intense storm complexes (Fritsch and Maddox, 1981a). Thus, further investigation of the role of the divergent wind component may be a fruitful method for exploring the effects of convection on the larger-scale environment.

As noted by Chen et al. (1978) current numerical prediction models generally reduce divergence (and therefore the divergent wind) in order to prevent spurious effects due to gravity waves. Current results, however, suggest that failure to adequately represent the divergent wind could lead to serious misrepresentations of the kinetic energy balance and possible errors in derived forecasts.

The results of this study suggest several areas for future investigation. Current findings should be verified with those from other storm outbreak cases. The use of subsynoptic scale data sets, such as those from AVE-SESAME '79, would be especially useful. In addition, the conversion of kinetic energy between rotational and divergent components should be explored to better

understand the formation of wind maxima near the storms. Krishnamurti and Ramanathan (1982) have shown that this process is important in producing monsoon circulations near India. The energetics team at Saint Louis University is actively pursuing these follow up studies.

APPENDIX

Sensitivity Analysis

Sensitivity of the energy budget to errors in the input rawinsonde data was evaluated quantitatively. Only the effects of random errors were considered, i.e., systematic errors and computational limitations were not investigated.

In several previous studies, random perturbations simulating rawinsonde errors have been introduced into the original station soundings. "Perturbed energy budgets" then were computed for comparison with original values (Vincent and Chang, 1975; Ward and Smith, 1976; Fuelberg and Scoggins, 1980; Robertson and Smith, 1980; Jedlovec and Fuelberg, 1981). In a recent investigation, Belt and Fuelberg (1982) documented the ability of their objective analysis and filtering procedures to decrease magnitudes of deliberately introduced sounding perturbations. They noted that standard deviations of height perturbations were reduced by approximately 30% at the grid points, while the more strongly filtered wind perturbations were reduced by approximately 50%. Since the objective analysis procedures of Belt and Fuelberg are almost identical to those of the present study (Section 3-b), an alternative technique for sensitivity analysis was devised that is based on their findings.

Our procedure was to introduce computer-generated random perturbations at the 42 computational grid points closest to corresponding rawinsonde stations. The perturbations then were

filtered horizontally so that effects of the "errors" were spread to surrounding grid points. By carefully selecting standard deviations of the input perturbations and their degree of filtering, it was possible to closely simulate the way that the Barnes objective analysis technique would have treated perturbations if they had been introduced at the stations themselves. Table 18 gives standard deviations for the normally distributed perturbations appearing in the final data grids for the current sensitivity study. These grid point values generally are either 30% or 50% smaller than station values proposed by Kurihara (1961) because current values reflect the ability of computational procedures to filter and thereby partially remove sounding errors.

The 0600 GMT 25 April observation was chosen for study since it was the time of maximum convective activity and greatest upper-level divergence. Ten sets of the 0600 GMT data, each with a different combination of perturbations at the individual 50 mb data levels, were made. The ten different sets should represent a good sample of situations that can be encountered with actual data. Figure 23 is an example of height perturbations at 200 mb. One should note that individual grid point deviations are as large as 75 m, considerably greater than values given in Table 18. This is possible because a normal distribution was allowed. Standard deviations (Table 18) and visual appearances of the height (Fig. 23) and wind perturbation (not shown) patterns show good agreement with those of Belt and Fuelberg (1982) and Jedlovec and Fuelberg (1981). Thus,

Table 18. Standard deviations of normally distributed grid point perturbations

Pressure Level (mb)	Wind Direction (deg)	Wind Speed ($m\ s^{-1}$)	Height (m)
100	5.3	2.5	30.2
200	4.5	2.2	24.2
300	3.4	1.8	15.5
500	6.1	1.0	8.1
700	1.5	0.7	7.0
900	9.2	0.7	3.1

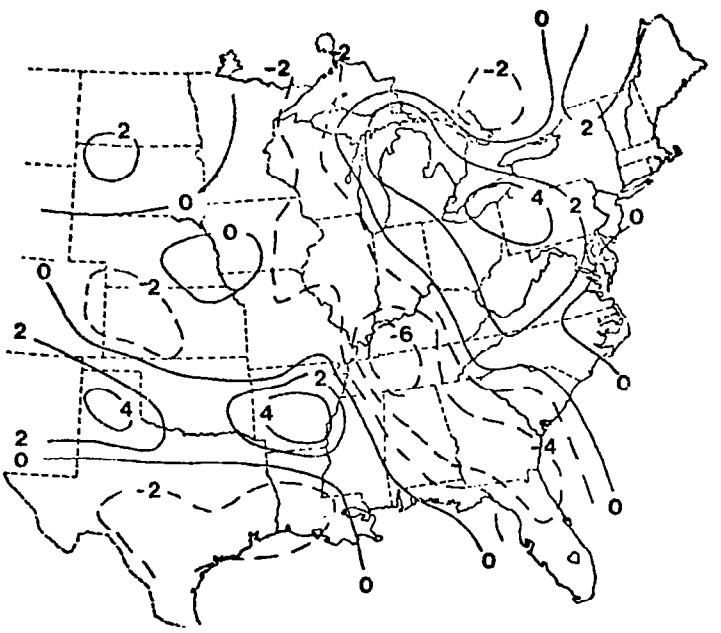

Fig. 23. Example of height perturbation field at 200 mb. Values are in tens of meters.

our sensitivity procedure should be a valid simple alternative to those cited initially. Since objective analysis is not required, the current procedure saves considerable computer time. Once the perturbed data grids were prepared, all subsequent procedures for computing the divergent wind, vertical motion, energy budgets, etc., were identical to those described in Section 3-b.

Mean absolute differences between the original area averaged budget at 0600 GMT and the ten budgets derived from the perturbed data are given in Table 19 for the entire region and in Table 20 for the limited volume enclosing MCC2 (Fig. 20). Results indicate that term sensitivity increases with altitude because the rawinsonde data were assumed to become less accurate at the higher levels. At any particular level, one can be more confident of the signs of terms having large values than those near zero. As noted by Jedlovec and Fuelberg (1981), mean absolute differences for the smaller area (Table 20) are somewhat larger than those for the entire region (Table 19); however, in most cases original values for the smaller area also are greater.

Quantities involving the divergent wind were somewhat less sensitive to data errors than expected. Belt and Fuelberg (1982) observed that strong, well defined patterns of horizontal divergence were not greatly affected by data errors. On the

Table 19. Area averaged kinetic energy budget and mean absolute differences (parentheses) for the entire computational region at 0600 GMT 25 April. Values of energy content are in 10^5 J m^{-2} while others are in W m^{-2}.

Pressure Layer (mb)	K_T	K_R	K_D	$\vec{V}_R \cdot \vec{V}_D$	$\partial K_T/\partial t$	$\partial \omega k/\partial p$	D
400-100	13.10	12.80	0.56	-0.20	0.4	-3.5	-2.8
	(0.17)	(0.14)	(0.04)	(0.02)	(0.2)	(0.3)	(1.3)
700-400	4.30	4.12	0.15	0.02	-2.4	2.4	3.0
	(0.05)	(0.05)	(0.01)	(0.0)	(0.2)	(0.3)	(0.5)
SFC-700	1.45	1.41	0.14	-0.09	-0.5	1.1	-0.8
	(0.02)	(0.01)	(0.0)	(0.0)	(0.0)	(0.0)	(0.1)
SFC-100	18.90	18.30	0.86	-0.26	-2.6	0.0	-0.6
	(0.18)	(0.16)	(0.05)	(0.02)	(0.2)	(0.0)	(1.4)

	$-\vec{V}_T \cdot \vec{\nabla}\phi$	$-\vec{V}_R \cdot \vec{\nabla}\phi$	$-\vec{V}_D \cdot \vec{\nabla}\phi$	$\vec{\nabla} \cdot k\vec{V}_T$	$\vec{\nabla} \cdot k\vec{V}_R$	$\vec{\nabla} \cdot k\vec{V}_D$
400-100	2.7	- 2.9	5.6	3.1	-1.1	4.1
	(1.2)	(0.7)	(0.5)	(0.7)	(0.5)	(0.3)
700-400	- 1.8	- 2.4	0.7	1.2	1.0	0.2
	(0.3)	(0.2)	(0.2)	(0.1)	(0.1)	(0.0)
SFC-700	1.8	1.4	0.4	0.4	0.5	-0.1
	(0.1)	(0.1)	(0.1)	(0.0)	(0.0)	(0.0)
SFC-100	2.7	- 4.0	6.7	4.7	0.5	4.3
	(1.2)	(0.8)	(0.6)	(0.7)	(0.5)	(0.3)

Table 20. Area averaged kinetic energy budget and mean absolute differences (parentheses) for the limited area enclosing MCC2 at 0600 GMT 25 April. Values of energy content are in 10^5 J m^{-2} while others are in W m^{-2}.

Pressure Layer (mb)	K_T	K_R	K_D	$\vec{V}_R \cdot \vec{V}_D$	$\partial K_T/\partial t$	$\partial \omega k/\partial p$	D
400-100	15.20	13.80	1.25	0.11	-2.1	-22.8	-13.5
	(0.32)	(0.26)	(0.06)	(0.08)	(0.6)	(1.2)	(4.0)
700-400	7.92	7.57	0.26	0.10	-3.2	18.0	- 1.5
	(0.13)	(0.13)	(0.01)	(0.03)	(0.6)	(1.1)	(2.2)
SFC-700	2.41	2.61	0.22	-0.41	-0.8	4.8	0.6
	(0.04)	(0.03)	(0.01)	(0.01)	(0.1)	(0.2)	(0.2)
SFC-100	25.50	24.00	1.73	-0.21	-6.2	0.0	-14.4
	(0.36)	(0.34)	(0.07)	(0.10)	(0.7)	(0.0)	(5.2)
	$-\vec{V}_T \cdot \vec{\nabla}\phi$	$-\vec{V}_R \cdot \vec{\nabla}\phi$	$-\vec{V}_D \cdot \vec{\nabla}\phi$	$\vec{\nabla} \cdot k\vec{V}_T$	$\vec{\nabla} \cdot k\vec{V}_R$	$\vec{\nabla} \cdot k\vec{V}_D$	
400-100	35.5	8.0	27.5	47.0	5.0	42.0	
	(2.9)	(1.8)	(1.4)	(4.5)	(2.1)	(2.8)	
700-400	15.6	5.4	10.2	- 0.8	1.3	- 2.1	
	(0.7)	(0.3)	(0.5)	(0.4)	(0.3)	(0.3)	
SFC-700	1.1	2.9	- 1.8	- 2.3	-0.7	- 1.7	
	(0.2)	(0.1)	(0.2)	(0.2)	(0.1)	(0.1)	
SFC-100	52.2	16.3	35.9	43.9	5.7	38.2	
	(3.3)	(1.8)	(1.7)	(4.3)	(2.0)	(2.9)	

other hand, weaker and less organized patterns were altered more significantly. Thus, in the present study, terms involving $\vec{V}_D$ would be smaller in magnitude and more sensitive to error at times other than 0600 GMT 25 April when 200 mb divergence reached 14×10^{-5} s^{-1}.

The sensitivity of field patterns was evaluated quantitatively by computing linear correlation coefficients between the original and ten perturbed budgets. Values were almost always greater than 0.95 for either area. Horizontal fields of several terms involving the divergent wind are given in Fig. 24 for the 400-100 mb layer. For each term, the diagram depicts the pattern having the lowest correlation of the ten runs. Corresponding original fields are shown in Figs. 9, 13 and 17. Generally, patterns for these "worst" cases show excellent agreements with their originals; however, magnitudes of some individual grid point values occasionally are altered significantly. For example, maximum grid point deviations in the 400-100 mb layer were 7.1×10^4 J m^{-2} for K_D, 49.3 W m^{-2} for HF_D, and 21.2 W m^{-2} for G_D.

In summary, random errors in rawinsonde data generally should not affect the interpretations of this study. Good space and time continuities of spatial patterns provide additional confidence.

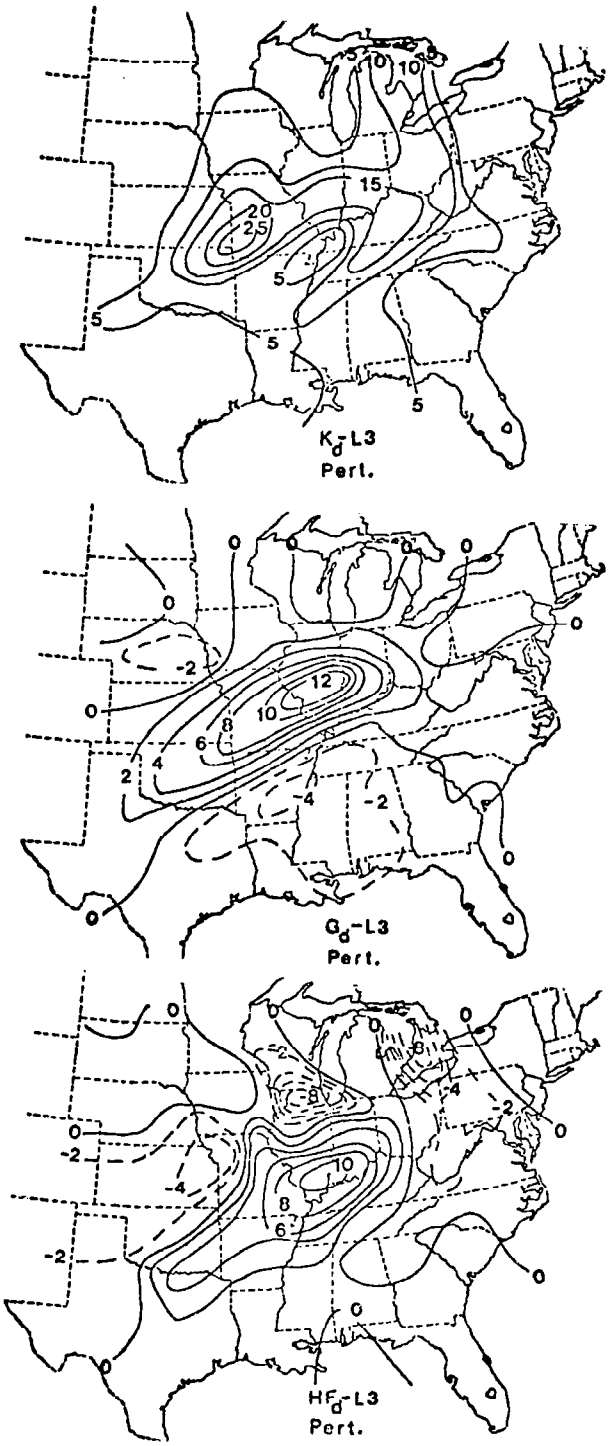

Fig. 24. Horizontal maps of the most perturbed fields for the 400-100 mb layer at 0600 GMT 25 April. Values of K_D are in 10^4 J m^{-2}, others are in 10^1 W m^{-2}.

BIBLIOGRAPHY

Aubert, E. J., 1957: On the release of latent heat as a factor in large-scale atmospheric motions. J. Meteor., 14, 527-542.

Barnes, S. L., 1964: A technique for maximizing detail in numerical map analysis. J. Appl. Meteor., 3, 396-409.

Belt, C. L., and H. E. Fuelberg, 1982: The effects of random errors in rawinsonde data on derived kinematic quantities. Mon. Wea. Rev., 110, 91-101.

Carlson, T. N., R. A. Anthes, M. Schwartz, S. G. Benjamin, and D. G. Baldwin, 1980: Analysis and prediction of severe storms environment. Bull. Amer. Meteor. Soc., 61, 1018-1032.

Charney, J. G., 1962: Intergration of the primitive and balance equations. Proc. Intern. Symp. Numerical Wea. Prediction, Meteor. Soc. of Japan, 131-152.

Chen, T. C., 1980: On the energy exchange between the divergent and rotational components of atmospheric flow over the tropics and subtropics at 200 mb during two northern summers. Mon. Wea. Rev., 108, 896-912.

Chen, T. C. and A. Wiin-Nielsen, 1976: On the kinetic energy of the divergent and nondivergent flow in the atmosphere. Tellus, 28, 486-498.

Chen, T. C., J. C. Alpert, and T. W. Schlatter, 1978: The effects of divergent and nondivergent winds on the kinetic energy budget of a mid-latitude cyclone: A case study. Mon. Wea. Rev., 106, 458-468.

Danard, M. B., 1964: On the influence of latent heat on cyclone development. J. Appl. Meteor., 3, 27-37.

Danard, M. B., 1966: On the contribution of released latent heat to changes in available potential energy. J. Appl. Meteor., 5, 81-84.

Dutton, J. A., and D. R. Johnson, 1967: The theory of available potential energy and a variational approach to atmospheric energetics. Advan. Geophys., 12, 333-436.

Endlich, R. M., 1967: An iterative method for altering the kinetic properties of wind fields. J. Appl. Meteor., 6, 837-844.

Fankhauser, J. C., 1969: Convective processes resolved by a mesoscale rawinsonde network. J. Appl. Meteor., 8, 778-798.

Fankhauser, J. C., 1974: The derivation of consistent fields of wind and geopotential height from mesoscale rawinsonde data. J. Appl. Meteor., 13, 637-646.

Fritsch, J. M., and C. F. Chappell, 1980a: Numerical prediction of convectively driven mesoscale pressure systems. Part I: Convective parameterization. J. Atmos. Sci., 37, 1722-1733.

Fritsch, J. M., and C. F. Chappell, 1980b: Numerical prediction of convectively driven mesoscale pressure systems. Part II: Mesoscale model. J. Atmos. Sci., 37, 1734-1762.

Fritsch, J. M., and R. A. Maddox, 1980: Analysis of upper-tropospheric mid-latitude mesoscale convective complexes. Preprints Eighth Conference on Weather Forecasting and Analysis, Denver, Amer. Meteor. Soc., 339-349.

Fritsch, J. M., and R. A. Maddox, 1981a: Convectively driven mesoscale weather systems aloft. Part I: Observations. J. Appl. Meteor., 20, 9-19.

Fritsch, J. M., and R. A. Maddox, 1981b: Convectively driven mesoscale weather systems aloft. Part II: Numerical simulations. J. Appl. Meteor., 20, 20-26.

Fucik, N. F., and R. E. Turner, 1975: Data for NASA's AVE IV experiment: 25-mb sounding data and synoptic charts. NASA TM X-64952. George C. Marshall Space Flight Center, AL, 458 pp.

Fuelberg, H. E., 1974: Reduction and error analysis of the AVE II pilot experiment data. NASA CR-120496, Marshall Space Flight Center, AL, 131 pp.

Fuelberg, H. E., E. M. Berecek, D. M. Ebel, and G. J. Jedlovec, 1980: Kinetic energy budgets in areas of intense convection. NASA CR-3336, George C. Marshall Space Flight Center, AL, 173 pp.

Fuelberg, H. E., and J. R. Scoggins, 1978: Kinetic energy budgets during the life cycle of intense convective activity. Mon. Wea. Rev., 106, 637-653.

Fuelberg, H. E., and J. R. Scoggins, 1980: Kinetic energy budget during strong jet stream activity over the eastern United States. Mon. Wea. Rev., 108, 69-77.

Jedlovec, G. J., and H. E. Fuelberg, 1981: A subsynoptic-scale kinetic energy study at the Red River Valley tornado outbreak (AVE-SESAME I). NASA CR-3456, George C. Marshall Space Flight Center, AL, 126 pp.

Kornegay, F. C., and D. C. Vincent, 1976: Kinetic energy budget analysis during interaction of tropical storm Candy (1968) with an extratropical frontal system. Mon. Wea. Rev., 104, 849-859.

Kreitzberg, C. W., and D. J. Perkey, 1977: Release of potential instability: Part II: The mechanism of convective mesoscale interaction. J. Atmos. Sci., 34, 1569-1595.

Krishnamurti, T. N., 1968: A study of a developing wave cyclone. Mon. Wea. Rev., 96, 208-217.

Krishnamurti, T. N., 1971: Observational study of the tropical upper-tropospheric motion field during the northern hemispheric summer. J. Appl. Meteor., 10, 1066-1096.

Krishnamurti, T. N., and Y. Ramanathan, 1982: Sensitivity of the monsoon onset to differential heating. J. Atmos. Sci., 39, 1290-1306.

Kung, E. C., and T. L. Tsui, 1975: Subsynoptic-scale kinetic energy balance in the storm area. J. Atmos. Sci., 32, 729-740.

Kurihara, Y., 1961: Accuracy of winds aloft data and estimation of errors in numerical analysis of atmospheric motions. J. Meteor. Soc. Japan, 39, 331-345.

Lin, S. C., and P. J. Smith, 1979: Diabatic heating and generation of available potential energy in a tornado producing extratropical cyclone. Mon. Wea. Rev., 107, 1169-1183.

Maddox, R. A., 1979: The evolution of middle and upper tropospheric features during a period of intense convective storms. Preprints Eleventh Conference Severe Local Storms, Kansas City, Amer. Meteor. Soc., 41-48.

Maddox, R. A., 1980a: A satellite based study of mid-latitude, mesoscale convective complexes. Preprints Eighth Conference on Weather Forecasting and Analysis, Denver, Amer. Meteor. Soc., 329-338.

Maddox, R. A., 1980b: Mesoscale convective complexes. Bull. Amer. Meteor. Soc., 61, 1374-1387.

Maddox, R. A., D. J. Perkey, and J. M. Fritsch, 1981: The evolution of upper-tropospheric features during the development of a mesoscale convective complex. J. Atmos. Sci., 38, 1664-1674.

Manabe, S., 1956: On the contribution of heat released by condensation to the change in pressure pattern. J. Meteor. Soc. Japan, 34, 12-24.

McInnis, D. H., and E. C. Kung, 1972: A study of subsynoptic-scale energy transformations. Mon. Wea. Rev., 100, 126-132.

Moore, J. T., and H. E. Fuelberg, 1981: A synoptic analysis of the first AVE-SESAME '79 period. Bull. Amer. Meteor. Soc., 62, 1577-1590.

Newell, R. E., D. G. Vincent, T. G. Dopplick, D. Ferruzza, and J. W. Kidson, 1970: The energy balance of the global atmosphere, in Global Circulation of the Atmosphere, edited by G. A. Corby, pp. 42-90, Roy. Met. Soc., London.

Ninomiya, K., 1971a: Dynamical analysis of outflow from tornado producing thunderstorms as revealed by ATS III pictures. J. Appl. Meteor., 10, 275-294.

Ninomiya, K., 1971b: Mesoscale modification of synoptic situations from thunderstorms as revealed by ATS III and aerological data. J. Appl. Meteor., 10, 1103-1121.

O'Brien, J. J., 1970: Alternate solution to the classical vertical velocity problem. J. Appl. Meteor., 9, 193-203.

Ogura, Y., and Y. Chen, 1977: A life history of an internal mesoscale convective storm in Oklahoma. J. Atmos. Sci., 34, 1458-1476.

Oort, A. H., and J. P. Peixóto, 1974: The annual cycle of the energetics of the atmosphere on a planetary scale. J. Geophys. Res., 79, 2705-2719.

Peixóto, J. P., and A. H. Oort, 1974: The annual distribution of atmospheric energy on a planetary scale. J. Geophys. Res., 79, 2149-2159.

Rao, G. V., and A. W. Hassebrock, 1972: Mesoscale latent heat release and its influence on mid-tropospheric warming. J. Appl. Meteor., 11, 1271-1283.

Robertson, F. R., and P. J. Smith, 1980: The kinetic energy budgets of two severe storm producing extratropical cyclones. Mon. Wea. Rev., 108, 127-143.

Saltzman, B., 1970: Large-scale atmospheric energetics in the wave number domain. Rev. Geophys. Space Phys., 8, 289-302.

Sanders, F., and K. A. Emanuel, 1977: The momentum budget and temporal evolution of a mesoscale convective system. J. Atmos. Sci., 34, 322-330.

Sanders, F., and R. J. Paine, 1975: The structure and thermodynamics of an intense mesoscale convective storm in Oklahoma. J. Atmos. Sci., 32, 1563-1579.

Sheu, J. P., and P. J. Smith, 1977: Kinetic energy budget analysis during a subperiod of the air mass transformation experiment 1975. Mon. Wea. Rev., 105, 1501-1507.

Shuman, F. G., 1957: Numerical methods in weather prediction: II. Smoothing and filtering. Mon. Wea. Rev., 85, 357-361.

Smith, P. J., 1969: On the contribution of a limited region to the global energy budget. Tellus, 21, 202-207.

Smith, P. J., 1974: Adjustments to the divergent component of the wind and their influence on synoptic scale, energy budget calculations. Preprints Fifth Conference Weather Forecasting and Analysis, St. Louis, Amer. Meteor. Soc., 152-155.

Smith, P. J., 1980: The energetics of extratropical cyclones. Rev. Geophys. Space Phys., 18, 378-386.

Smith, P. J. and S. C. Lin, 1980: The generation and release of available potential energy in an extratropical cyclone. Preprints Eighth Conference Weather Forecasting and Analysis, Denver, Amer. Meteor. Soc., 346-350.

Tsui, T. L., and E. C. Kung, 1977: Subsynoptic-scale energy transformations in various severe storm situations. J. Atmos. Sci., 34, 98-110.

Vincent, D. G., and L. N. Chang, 1975: Kinetic energy budgets of moving systems. Case studies for an extratropical cyclone and hurricane Celia, 1970. Tellus, 27, 215-233.

Vincent, D. G., and T. W. Schaltter, 1979: Evidence of deep convection as a source of synoptic-scale kinetic energy. Tellus, 31, 493-504.

Ward, J. H., and P. J. Smith, 1976: A kinetic energy budget over North America during a period of short synoptic wave development. Mon. Wea. Rev., 104, 836-848.

Wilson, G. S., 1976: Large-scale vertical motion calculations in the AVE IV experiment. Geophys. Res. Lett., 3, 735-740.

1. REPORT NO.	2. GOVERNMENT ACCESSION NO.	3. RECIPIENT'S CATALOG NO.
NASA CR-3702		

4. TITLE AND SUBTITLE	5. REPORT DATE
Contributions of Divergent and Nondivergent Winds to the Kinetic Energy Balance of a Severe Storm Environment	June 1983
	6. PERFORMING ORGANIZATION CODE
7. AUTHOR(S)	8. PERFORMING ORGANIZATION REPORT #
Peter A. Browning and Henry E. Fuelberg	
9. PERFORMING ORGANIZATION NAME AND ADDRESS	10. WORK UNIT NO.
Department of Earth and Atmospheric Sciences Saint Louis University Saint Louis, Missouri 63103	M-414
	11. CONTRACT OR GRANT NO.
	NAS8-33370
12. SPONSORING AGENCY NAME AND ADDRESS	13. TYPE OF REPORT & PERIOD COVERED
National Aeronautics and Space Administration Washington, D.C. 20546	Contractor Report (Interim Report)
	14. SPONSORING AGENCY CODE

15. SUPPLEMENTARY NOTES

Prepared for Marshall Space Flight Center, Science and Engineering Directorate, Space Science Laboratory, Atmospheric Sciences Division
Marshall Technical Monitor: Gregory S. Wilson

16. ABSTRACT

Divergent and rotational components of the synoptic-scale kinetic energy balance are presented using rawinsonde data at 3 and 6 h intervals from NASA's fourth Atmospheric Variability Experiment (AVE 4) conducted on April 24-25, 1975. Two intense thunderstorm complexes occurred during the period. Energy budgets are described for the entire computational region and for limited volumes that enclose and move with the convection.

Although small in magnitude, the divergent wind component played an important role in the cross-contour generation and horizontal flux divergence of kinetic energy. The importance of $\bar{V}_D$ appears directly to the presence and intensity of convection within the area. Although K_D usually comprised less than 10 percent of the total kinetic energy content within the storm environment, as much as 87 percent of the total horizontal flux divergence and 68 percent of the total cross-contour generation was due to the divergent component in the upper atmosphere. Generation of kinetic energy by the divergent component appears to have been a major factor in the creation of an upper-level wind maximum on the poleward side of one of the complexes. A random error analysis is presented to assess confidence limits in the various energy parameters.

17. KEY WORDS	18. DISTRIBUTION STATEMENT
Divergent Winds Non-divergent Winds Kinetic Energy Balance Severe Storm Environment Upper level winds rotational wind component	Unclassified - Unlimited Subject Category 47

19. SECURITY CLASSIF. (of this report)	20. SECURITY CLASSIF. (of this page)	21. NO. OF PAGES	22. PRICE
Unclassified	Unclassified	115	A06

For sale by National Technical Information Service, Springfield, Virginia 22161

NASA-Langley, 1983